

Supermassive Black Hole Winds in X-rays – SUBWAYS. I. Ultra-fast outflows in QSOs beyond the local Universe

G. A. Matzeu^{1,2,3,*}, M. Brusa^{1,2}, G. Lanzuisi², M. Dadina², S. Bianchi⁴, G. Kriss⁵, M. Mehdipour⁵, E. Nardini⁶, G. Chartas⁷, R. Middei⁸, E. Piconcelli⁹, V. Gianolli^{4,10}, A. Comastri², A. L. Longinotti¹¹, Y. Krongold¹¹, F. Ricci⁴, P. O. Petrucci¹⁰, F. Tombesi^{12,9,13,14}, A. Luminari^{15,9}, L. Zappacosta⁹, G. Miniutti¹⁶, M. Gaspari¹⁷, E. Behar¹⁸, M. Bischetti¹⁹, S. Mathur^{20,21}, M. Perna¹⁶, M. Giustini¹⁶, P. Grandi², E. Torresi², C. Vignali^{1,2}, G. Bruni¹⁵, M. Cappi², E. Costantini²², G. Cresci⁶, B. De Marco²³, A. De Rosa¹⁵, R. Gilli², M. Guainazzi²⁴, J. Kaastra^{22,25}, S. Kraemer²⁶, F. La Franca⁴, A. Marconi²⁷, F. Panessa¹⁵, G. Ponti²⁸, D. Proga²⁹, F. Ursini⁴, F. Fiore¹⁹, A. R. King³⁰, R. Maiolino³¹, G. Matt⁴, and A. Merloni³²

(Affiliations can be found after the references)

December 7, 2022

ABSTRACT

We present a new X-ray spectroscopic study of 22 luminous ($2 \times 10^{45} \lesssim L_{\text{bol}}/\text{erg s}^{-1} \lesssim 2 \times 10^{46}$) active galactic nuclei (AGNs) at intermediate-redshift ($0.1 \lesssim z \lesssim 0.4$), as part of the Supermassive Black hole Winds in the x-RAYS (SUBWAYS) sample, mostly composed of quasars (QSOs) and type 1 AGN. Here, 17 targets were observed with *XMM-Newton* between 2019–2020 and the remaining 5 are from previous observations. The aim of this large campaign (1.45 Ms duration) is to characterise the various manifestations of winds in the X-rays driven from supermassive black holes in AGN. In this paper we focus on the search and characterization of ultra-fast outflows (UFOs), which are typically detected through blueshifted absorption troughs in the Fe K band ($E > 7$ keV). By following Monte Carlo procedures, we confirm the detection of absorption lines corresponding to highly ionised iron (e.g., Fe xxv He α , Fe xxvi Ly α) in 7/22 sources at the $\geq 95\%$ confidence level (for each individual line). The global combined probability of such absorption features in the sample is $> 99.9\%$. The SUBWAYS campaign extends at higher luminosity and redshifts than previous local studies on Seyferts, obtained using *XMM-Newton* and *Suzaku* observations. We find a UFO detection fraction of $\sim 30\%$ on the total sample that is in agreement with the previous findings. This work independently provides further support for the existence of highly-ionised matter propagating at mildly relativistic speed ($\geq 0.1c$) in a considerable fraction of AGN over a broad range of luminosities, which is expected to play a key role in the self-regulated AGN feeding-feedback cycle, as also supported by hydrodynamical multiphase simulations.

Key words. galaxies: active – galaxies: nuclei – X-rays: galaxies

1. Introduction

It is widely accepted that supermassive black holes (SMBHs, $10^6 - 10^{10} M_{\odot}$, e.g., Salpeter 1964; Magorrian et al. 1998) are hosted at the centre of virtually every known massive galaxy. The observed tight correlations between the host galaxy and the SMBH properties (see Kormendy & Ho 2013, for a review) strongly suggest that their formation and evolution are profoundly coupled with each other. Some physical mechanisms must have therefore linked the regions where the SMBH gravitational field dominates to the larger scales, where its direct influence is negligible. At this stage, the key underlying ingredients at play in the co-evolution paradigms of Active Galactic Nuclei (AGN) and galaxies still need to be understood. It has been proposed that highly ionised gas outflows could play a pivotal role in this process (e.g., King 2003, 2005; Gaspari & Sądowski 2017). The presence of such powerful winds is expected to regulate accretion of material onto (and ejection from) compact objects.

Through their mechanical power, ultra-fast outflows (UFOs) are accelerated at velocities larger than $10,000 \text{ km s}^{-1}$ and up to a few tens of the speed of light. For these reasons, UFOs are also able to inject momentum and energy over wide spatial scales via the interaction with the inter-stellar medium (ISM) in the host galaxy. This process is expected to promote an efficient

feedback mechanism (e.g., Murray et al. 2005; Di Matteo et al. 2005; Ostriker et al. 2010; Torrey et al. 2020), that is needed to reproduce the observed properties in galaxies, e.g. the scaling relations (King et al. 2011), and to regulate their overall mass-size ecosystem (e.g., Fabian 2012; King & Pounds 2015; Heckman & Best 2014).

UFOs are routinely detected in the X-ray spectra of 30–40% of local ($z \lesssim 0.1$) AGN (Tombesi et al. 2010; Gofford et al. 2013; Igo et al. 2020, hereafter T10; G13; Igo20), and in a handful of sources at intermediate to high redshift (up to $z \sim 3$; e.g., Chartas et al. 2002; Lanzuisi et al. 2012; Chartas et al. 2021, hereafter C21). UFOs manifest themselves as absorption troughs associated with Fe xxv He α and Fe xxvi Ly α transitions ($E_{\text{rest}} = 6.7 - 6.97$ keV) blueshifted at energies $E_{\text{rest}} > 7$ keV (all the line energies will be given in the source rest-frame throughout this work). The degree of blueshift translates into the range of extreme outflow velocities observed between $v_{\text{out}} \sim -0.03c$ up to $-0.5c$, for gas column densities and ionisations of $N_{\text{H}} \sim 10^{23-24} \text{ cm}^{-2}$ and $\log(\xi/\text{erg cm s}^{-1}) \geq 3$, respectively (e.g., Reeves et al. 2003; Pounds & Reeves 2009; Tombesi et al. 2011; Matzeu et al. 2017; Reeves et al. 2018a; Parker et al. 2018; Braito et al. 2018). The frequent detection of these features, supported by a detailed modelling of the high energy spectra of the most powerful local QSO hosting X-ray winds, PDS 456, indicates that UFOs arise in wide

* gabriele.matzeu@unibo.it

angle outflows, implying that a significant amount of kinetic power is involved (Nardini et al. 2015; Luminari et al. 2018).

Evidence for low-ionisation UFO components have been also reported in the soft X-ray spectra in the $E_{\text{rest}} = 0.3\text{--}2$ keV band (e.g., Braito et al. 2014; Longinotti et al. 2015; Reeves et al. 2016, 2018b; Serafinelli et al. 2019; Reeves et al. 2020; Krongold et al. 2021), usually observed as blueshifted oxygen and neon ions. Similar high-velocity outflows, arising directly from the accretion disc region, have also been found in the UV spectra via prominent blueshifted, ionised absorption and emission features in broad absorption line quasars (BAL QSOs), typically between $\lambda_{\text{rest}} = 50\text{--}2000$ Å (e.g., Gaskell 1982; Wilkes & Elvis 1987; Richards et al. 2011). These are associated with lower ionisation metal ions (C IV, Al II, Fe II, etc; e.g. Crenshaw et al. 2003; Green et al. 2012; Hamann et al. 2018; Kriss et al. 2018, 2019; Mehdipour et al. 2022; Vietri et al. 2022). It has been shown that at least some of the UV absorbing outflows in sub-Eddington systems can be driven by radiation pressure on spectral lines (e.g., Murray et al. 1995; Proga et al. 2000). We refer to the recent review by Giustini & Proga (2019) for more details.

Outflowing material at considerably lower velocity (typically within a v_{out} of ~ 5000 km s $^{-1}$) and less ionised than UFOs at $\log(\xi/\text{erg cm s}^{-1}) \sim 1 - 3$ (e.g., Sako et al. 2000; Parker et al. 2019a), known as a warm absorber (WA), is also detected through absorption features and edges from He- or/and H-like ions of C, O, N, Ne, Mg, Al, Si and S in the X-rays (Halpern 1984; Mathur et al. 1997, 1998; Blustin et al. 2005; Reeves et al. 2013; Kaastra et al. 2014; Laha et al. 2014, 2016). WAs are detected in a substantial fraction of AGN, i.e. $\sim 65\%$ (Reynolds 1997; Piconcelli et al. 2005; McKernan et al. 2007). It was suggested by Tombesi et al. (2013) that despite their physical distinction, UFOs and WAs might be connected somehow as part of the same wind, but originating from different locations (see Laha et al. 2021 for a comprehensive review of ionised outflows).

Finally, outflowing gas is also routinely observed at host-galaxy scales, in the ionised, neutral/atomic and molecular phases. These outflowing components observed at kpc scale or beyond are now traced with modern sensitive optical/far-IR/mm/radio facilities (e.g., Morganti et al. 2005; Feruglio et al. 2010; Harrison et al. 2014; Brusa et al. 2015; Maiolino et al. 2012; Cresci et al. 2015; Feruglio et al. 2017; Brusa et al. 2018; Bischetti et al. 2019a) and show lower velocities with respect to the accretion disc winds ($v_{\text{out}} \sim -500$ to -2000 km s $^{-1}$, depending on the phase), and considerably higher mass outflow rates up to $100\text{--}1000 M_{\odot}/\text{yr}$ (see Cicone et al. 2018).

Some models predict that the fast outflowing gas is accelerated by the radiation pressure caused by highly accreting black holes approaching the Eddington limit (e.g. Zubovas & King 2012). Subsequently, the energy deposited via shocks by the UFO into the galaxy ISM generates the galaxy-wide outflows observed in lower-ionisation gas (see Fabian 2012; King & Pounds 2015). Alternatively, massive sub-relativistic outflows are expected also in systems accreting at lower Eddington ratio, due to magnetic (e.g., Fukumura et al. 2010, 2017; Kraemer et al. 2018) and/or thermal driving (e.g., Woods et al. 1996; Mizumoto et al. 2019; Waters et al. 2021). The global AGN feeding-feedback self-regulated framework has been supported by three-dimensional hydrodynamical simulations unifying the micro and macro properties of the AGN environment (e.g., Gaspari et al. 2013, 2020; Sądowski & Gaspari 2017; Yang et al. 2019; Wittor & Gaspari 2020), which, in turn, have been corroborated by several multi-wavelength observations (e.g., Maccagni et al. 2021; Eckert et al. 2021; McKinley et al. 2022; Temi et al. 2022).

Multi-phase tracers would therefore allow us to probe galactic outflows in their full extent, that is, from the nuclear (< 1 pc) to the largest scales (> 10 kpc), and at the same time to have a comprehensive view of their driving mechanism. Fiore et al. (2017) reported a correlation between the velocity of the wind (for both UFOs and large-scale components) and the bolometric luminosity, ($L_{\text{bol}} \propto v_{\text{out}}^{3.9}$), in agreement with that predicted by Costa et al. (2014) for energy conserving outflows. However, the statistics of this work for the UFO sample is still limited (~ 20 AGN with UFOs), with only 50% at $L_{\text{bol}} \gtrsim 10^{45}$ erg s $^{-1}$.

A comparison between the momentum rates (i.e., $\dot{p}_{\text{out}} = \dot{M}_{\text{out}} v_{\text{out}}$) observed over a range of spatial scales can be used to disentangle the wind propagation mechanisms, i.e. energy (large-scale) vs. momentum (small-scale: UFO) conserving. The first reported cases of molecular outflows in systems hosting an UFO are: IRAS F11119+3257 (Tombesi et al. 2015), Mrk 231 (Feruglio et al. 2015), IRAS 17020+4544 (Longinotti et al. 2015, 2018) and APM 08279+5255 (Feruglio et al. 2017), supporting the energy-driven wind scenario, deemed as the smoking gun for a large scale feedback. Indeed, conserving energy is crucial to achieve an effective macro-scale feedback to quench cooling flows and star formation (e.g., Gaspari et al. 2019). However, by analysing more sources, it emerged that not all the outflows supported this scenario. Further molecular outflows observed in UFO hosting sources, such as PDS 456 (Bischetti et al. 2019b), MCG-03-58-007 (Sirressi et al. 2019), IZwicky 1 (Cicone et al. 2014; Reeves & Braito 2019) and Mrk 509 (Zanchettin et al. 2021) revealed momentum rates at least two orders of magnitude below the expected value for an energy conserving wind (see also Marasco et al. 2020; Tozzi et al. 2021). These results are suggesting a more complex physical mechanism and range of efficiencies in transferring the nuclear wind out to the large-scale galaxy structure, or significant AGN variability over the lifetime of the flow (Nardini & Zubovas 2018; Zubovas & Nardini 2020), as supported by Chaotic Cold Accretion (CCA) simulations (Gaspari et al. 2017). Related to this, an important parameter that is needed to constrain wind models is the UFO duty cycle, i.e. how persistent accretion disc winds are. Indeed, the derivation of the energy injection rate by UFOs into the galaxy ISM must take into account this factor, with implications for the timescale and efficiency of propagation through the host galaxy (Zubovas & King 2016). The UFO duty cycle can be inferred from the fraction of AGN in which they are observed, but it is highly degenerate with the opening angle, hence, as of today, it is virtually unconstrained for sources above $L_{\text{bol}} \sim 10^{45}$ erg s $^{-1}$. Observing large samples of sources at luminosities above the break $L \gtrsim L^*$ of the AGN luminosity function (e.g., Aird et al. 2015), with a range of Eddington ratios and enough statistics to constrain the wind duty cycle, has become crucial to overcome the limitations described above (e.g., Bertola et al. 2020).

This work is the first of a series of SUBWAYS publications, with the dedicated goals of investigating the various manifestations of UFOs emanating from the environments of supermassive black holes in AGNs. These include: (i) gaining significant advances in our understanding of the detection rate and physical properties of UFOs and (ii) their connection with WA features, as well as (iii) their role in providing a macro-scale feedback and finally (iv) mapping the physical properties of the outflows across different galaxy scales and gas phases at different wavelengths/ionisation states. In this paper we present our first results of the SUBWAYS campaign, specifically designed to provide a solid detection of blueshifted absorption features in the Fe K band in context of a robust statistical grounds for high signal-to-noise ratio (SNR hereafter) sources at $L \gtrsim 10^{45}$ erg s $^{-1}$.

The paper is organised as follows: Section 2 presents the SUBWAYS sample and the target selection. In Section 3 we describe the reduction of the *XMM-Newton* data. In Section 4 we present all the details of the spectral analysis of the EPIC data, including the continuum modeling, the procedure we adopted to search for Fe K emission and absorption features, the modeling of the Fe K band and the Monte Carlo simulations we used to assign a robust significance level to the detections. In Section 5 we present our main results, i.e. the line detection rate as inferred from our spectral modeling, and in Section 6 we discuss our findings in the light of recent results at both lower and higher redshift; Section 7 summarises our results. Cosmological values of $H_0 = 70 \text{ km s}^{-1} \text{ Mpc}^{-1}$, $\Omega_{\Lambda_0} = 0.73$ and $\Omega_M = 0.27$ are assumed throughout this paper, and errors are quoted at the 90 percent confidence level or a difference in C-statistic (Cash 1979, i.e., $\Delta C = 2.71$) for one parameter of interest, unless otherwise stated. The cosmic abundances are set to solar throughout the paper.

2. The SUBWAYS campaign

So far the characterisation of the fastest components of accretion disc winds has been mainly carried out through studies based on inhomogeneous archival data, restricted to two distinct cosmic epochs and luminosity regimes, merely for practical reasons: (i) at $z < 0.1$, objects are close enough that it is relatively easy to collect $> 5\text{--}10 \times 10^3$ counts in the 4–10 keV band in large samples (~ 50 objects), but mainly limited to Seyfert luminosities ($L_{\text{bol}} \lesssim 10^{45} \text{ erg s}^{-1}$, e.g., T10; G13; Igo20); (ii) at $z \gtrsim 1.5$, on small and sparse samples (< 10 objects) at $L_{\text{bol}} \gtrsim 10^{46} \text{ erg s}^{-1}$, which are mostly composed of gravitationally lensed objects (e.g., Chartas et al. 2009; Vignali et al. 2015; Dadina et al. 2016, C21). The distribution of these two samples in the L – z plane is shown in the upper panel of Figure 1 (blue and magenta points, respectively).

In order to gain significant advances in our understanding of the physical properties of UFOs in the quasi stellar object (QSO)-like regime, a systematic approach is needed. The SUBWAYS sample consists of a total of 22 radio-quiet X-ray AGN, mostly Type 1 and QSOs, where 17 sources have been observed with *XMM-Newton* (Jansen et al. 2001) between May 2019 and June 2020 (see Table 1) as part of a large program (1.45 Ms, PI: M. Brusa) awarded in 2018 (cycle AO18 LP). In addition, the sample includes the data of 5 sources that meet the L – z –counts selection criteria (see below) already available in the archive¹. A companion SUBWAYS Paper II (mehdipour et al. 2022; in press) is primarily focused on the UV outflow spectroscopic analysis of Cosmic Origins Spectrograph (COS, Green et al. 2012) data as part of a large complementary SUBWAYS observational campaign carried out with the Hubble Space Telescope (HST).

The SUBWAYS selection criteria are based on the following requirements:

1. presence of the source in the 3XMM-DR7 catalog², matched to the SDSS-DR14 catalog³, or to the Palomar-Green Bright QSO catalog (PG QSO; Schmidt & Green 1983);
2. intermediate redshift in the range, $z = 0.1\text{--}0.4$. This condition ensures that both WAs and UFOs can be studied at the same time, and provides the possibility to characterise the continuum up to 10 keV. Indeed, in order to recognise faint

¹ In this analysis we discarded all observations with a net count threshold of ≤ 1500 in the 4–10 keV band.

² http://xmmssc.irap.omp.eu/Catalogue/3XMM-DR7/3XMM_DR7.html

³ <http://www.sdss.org/dr14/>

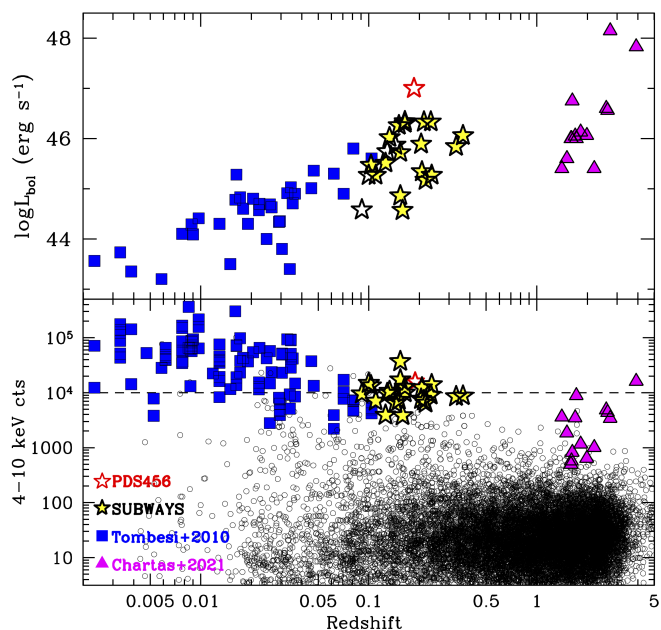


Fig. 1: Luminosity (upper panel) and rest frame 4–10 keV counts (lower panel) plotted against redshift for the objects in the SUBWAYS sample and the comparison samples (T10; C21), as labelled. In the lower panel we also mark as small empty circles the sources of the 3XMM sample, used to select the SUBWAYS targets.

absorption features, it is key to achieve a good handling of the continuum in spectra with high counting statistics up to 10 keV;

3. count rate larger than ~ 0.12 cts/s, in order to ensure counts of the order of $\sim 10^4$ in the 4–10 keV band in the EPIC-pn spectra, obtained within a single *XMM-Newton* orbit. A by-product of this requirement also implies that our targets are QSOs ($L_{\text{bol}} \gtrsim 10^{45} \text{ erg s}^{-1}$; star points in Figure 1), complementing the data already available in the archives for this kind of studies;
4. we discarded Narrow Line Seyfert 1 (NLSy1s) due to the highly variable EPIC count rate, and QSOs in clusters/radio loud systems, in order to avoid contamination by processes other than AGN accretion and UFOs.

The lower panel of Figure 1 shows the currently available rest-frame 4–10 keV counts for the SUBWAYS sample (large stars), compared to those in 3XMM-SDSS, 3XMM-PGQSO and local and high- z QSOs UFO samples (see labels and caption for details). In this paper, we will focus specifically on the detection and characterization of blueshifted absorption profiles in the Fe K band in the 17 newly observed sources plus the additional 5 from previous observations (up to AO18 cycle), for a total of 22 targets. The properties of the targets are listed in Table 1.

3. Data reduction

In this work we focus on the EPIC-pn (Strüder et al. 2001), EPIC-MOS 1 and MOS 2 (Turner et al. 2001) data. They were processed and cleaned by adopting the Science Analysis System SAS v18 (Gabriel et al. 2004) and the up-to-date calibration files. We initially checked for Cu instrumental emission in the EPIC-pn CCDs, between 7–8.5 keV and 7.8–8.2 keV, for the source

Table 1: Target properties of the large SUBWAYS campaign. Columns: (1) Target name; (2) Redshift; (3) Galactic absorption measured by [HI4PI Collaboration et al. \(2016\)](#) or [Murphy et al. \(1996\)](#)[†]; (4) 2–10 keV intrinsic luminosity measured in this work by using the `cLumin` convolution model in `XSPEC`; (5) bolometric luminosity derived from the X-ray luminosity assuming the bolometric correction of [Duras et al. \(2020\)](#); (6) log of black hole mass from the measurements carried out in [Bianchi et al. \(2009\)](#)^a, [Xie et al. \(2017\)](#)^b, [Perna et al. \(2017\)](#)^c, [Kaspi et al. \(2000b\)](#)^d and this work^e; (7) Eddington ratio; (8) 2–10 keV fluxes from the available spectra measured with `cFlux` in `XSPEC`. The L_X and L_{bol} measured in this work are consistent with the ones that were used during the SUBWAYS selection process.

Name (1)	z (2)	$N_{\text{H}}^{\text{Gal}}$ (3)	$\log L_X$ (4)	$\log L_{\text{bol}}$ (5)	$\log M_{\text{BH}}$ (6)	$\log L_{\text{bol}}/L_{\text{Edd}}$ (7)	$\log F_{2-10\text{keV}}$ (8)
		10^{20} cm^{-2}	erg s^{-1}	erg s^{-1}	M_{\odot}		$\text{erg cm}^{-2} \text{ s}^{-1}$
PG0052+251	0.15445	3.96	44.609 ± 0.003	46.00	8.41 ^a	-0.51	-11.204 ± 0.003
PG0953+414	0.23410	1.09	44.595 ± 0.004	46.08	8.24 ^a	-0.26	-11.664 ± 0.004
PG1626+554	0.13170	1.55 [†]	44.076 ± 0.004	45.42	8.54 ^a	-1.22	-11.600 ± 0.004
PG1202+281	0.16501	1.74	44.400 ± 0.004	45.77	8.61 ^a	-0.94	-11.469 ± 0.004
PG1435-067	0.12900	4.84	43.684 ± 0.007	44.98	7.77 ^b	-0.89	-11.962 ± 0.007
SDSSJ144414+0633	0.20768	2.57	44.467 ± 0.004	45.84	8.10 ^c	-0.36	-11.634 ± 0.004
2MASXJ165315+2349	0.10300	4.15	43.790 ± 0.006	45.37	6.98 ^e	0.29	-11.529 ± 0.007
PG1216+069	0.33130	1.51	44.769 ± 0.004	46.24	9.20 ^a	-1.06	-11.810 ± 0.005
PG0947+396 (Obs1)	0.20553	1.91 [†]	44.208 ± 0.007	45.55	8.68 ^a	-1.24	-11.887 ± 0.008
PG0947+396 (Obs2)	0.20553	1.91 [†]	44.146 ± 0.006	45.55	8.68 ^a	-1.24	-11.954 ± 0.007
WISEJ053756-0245	0.11000	15.0	43.688 ± 0.005	44.86	7.73 ^c	-0.97	-11.777 ± 0.006
HB891529+050	0.21817	3.93	44.219 ± 0.005	45.52	8.75 ^c	-1.33	-11.918 ± 0.005
PG1307+085	0.15384	2.10	44.312 ± 0.003	45.70	7.90 ^a	-0.30	-11.512 ± 0.003
PG1425+267	0.36361	1.57	44.823 ± 0.004	46.31	9.22 ^c	-1.01	-11.823 ± 0.005
PG1352+183	0.15147	1.55	43.889 ± 0.004	45.21	8.42 ^a	-1.31	-11.921 ± 0.005
2MASXJ105144+3539 ^e	0.15900	2.20	43.692 ± 0.008	44.88	8.40 ^c	-1.62	-12.068 ± 0.009
2MASXJ0220-0728	0.21343	2.42	44.213 ± 0.005	45.51	8.42 ^c	-1.01	-11.888 ± 0.006
LBQS1338-0038	0.23745	1.68	44.520 ± 0.003	45.91	7.77 ^c	0.04	-11.707 ± 0.004
Archival targets							
PG0804+761 ^d	0.10000	7.09	44.330 ± 0.002	45.71	8.31 ^d	-0.33	-11.087 ± 0.003
PG1416-129	0.12900	3.34	44.170 ± 0.005	45.58	9.05 ^a	-1.57	-11.447 ± 0.005
PG1402+261	0.16400	1.22	44.030 ± 0.004	45.39	7.94 ^a	-0.65	-11.874 ± 0.004
HB89 1257+286	0.09100	1.04	43.551 ± 0.002	45.15	7.46 ^c	-0.41	-11.831 ± 0.002
PG1114+445	0.14400	1.93 [†]	44.088 ± 0.003	45.53	8.59 ^a	-1.16	-11.602 ± 0.003

extraction and subsequent high-background screening. We followed the [Piconcelli et al. \(2004\)](#) optimised procedure aimed at maximizing the SNR in the 4–10 keV band (in the EPIC-pn), rather than using the conservative criterion based on the fiducial rejection of time-intervals of high-background count rates (i.e., between 10–12 keV). The SNR optimization procedure is necessary to identify any absorption feature that would otherwise be diluted (e.g., [Nardini et al. 2019](#)), but insufficient if this does not also correspond to the optimal compromise between SNR and number of counts.

Given the relatively small EPIC-MOS collecting area at $E_{\text{obs}} \geq 4 \text{ keV}$, a 4–10 keV band optimization would remove too many counts; we then optimised the filtering on the entire 0.3–10 keV band. Apart from the different reference bands, the applied method is the same for the pn and MOS instruments. We selected a background region free of instrumental features. These regions have dimensions of 40 or 50 arcsec depending on the possibility, for each observation, to find source-free regions on the detectors. In order to define the source regions different extraction radii were tested and for each radius we calculated the maximum level of background that can be tolerated in order to find the optimal SNR. Following [Piconcelli et al. \(2004\)](#), we define this level of background as Max Background (see Appendix A for more details). The EPIC source spectra were individually inspected for the possible presence of photon pile-up by using the SAS task `EPATPLOT`. The ratios of singles to double pixel events

were found to be within 1% of the expected nominal values, and thus no significant pile-up is present. The response files were subsequently generated with the SAS tasks `RMFGEN` and `ARFGEN` with the calibration EPIC files version v3.12. In [Table B.1](#) we show a summary of the individual observations of the 22 SUBWAYS targets that were selected adopting a threshold of ≥ 1500 EPIC-pn net counts in the 4–10 keV band.

4. Spectral Analysis

The pioneering UFO studies were conducted on large archival samples of AGN. More specifically, [T10](#) carried out a systematic hard-band (i.e., 3.5–10.5 keV) analysis on a sample of 42 sources (for a total of 101 observations), drawn from the archival *XMM-Newton* EPIC data, to carry out a blind search of Fe xxv $\text{He}\alpha$ and Fe xxvi $\text{Ly}\alpha$ absorption lines. By analyzing the data of 51 AGN, obtained with the *Suzaku* observatory, [G13](#) constructed broadband spectral models over the entire band-pass, i.e. 0.6–10 keV.

For a robust analysis, we choose, as per [G13](#), the entire EPIC band-pass, where additional spectral complexities like warm absorbers and/or strong soft excesses can also be taken into account. In this way we ensure that all our models accurately describe the overall continuum. We focus on the *XMM-Newton* EPIC-pn, MOS 1 and MOS 2 data in the 0.3–10 keV range. We applied a blind-search procedure in each of the 41 observations by adopting

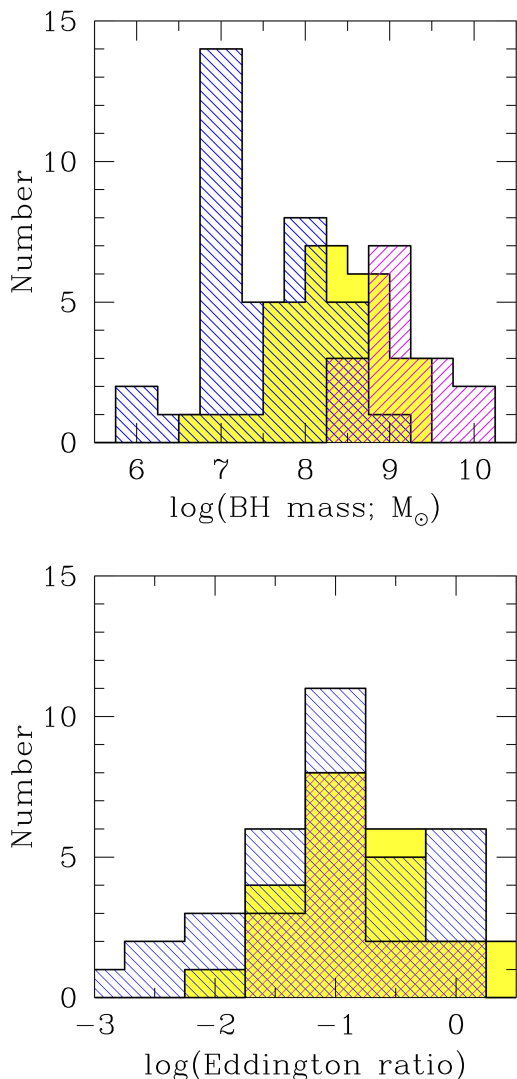


Fig. 2: The BH mass and Eddington ratio distributions of our targets (see Table 1) and the comparison samples. The color scheme for the samples is the same as in Figure 1.

four spectral binning methods (for a total of 164 blind-searches; see Appendix C for details). These binnings are: `grpmin1`, `SN5`, `OS3grp20`, by using the `SAS` routine `SPECGROUP`, and the optimal binning of Kaastra & Bleeker (2016, \mathcal{KB} hereafter), by using the `HEASOFT` routine `FTGROUPPHA`.

We find that the spectral resolution delivered by the `SN5` and `OS3grp20` binning methods is too degraded compared to the `grpmin1` and \mathcal{KB} ones, and therefore not suitable for the detection of faint, narrow absorption and emission features. The `grpmin1` and \mathcal{KB} criteria produce nearly identical results, in terms of detection rate and statistical significance of the features. While `grpmin1` would certainly be a more conservative option, we finally chose the \mathcal{KB} binning, which is specifically developed to optimise the SNR in narrow, unresolved spectral features whilst maintaining the necessary spectral resolution. Such a choice provided the right compromise between these binning methods. In other words, Kaastra & Bleeker (2016) worked out a binning scheme based on the resolution of the detector and the available number of photons at the energy of interest. Such a method

allowed us to maximise the information provided by the Fe K absorption lines, and in this framework we adopted a maximum likelihood statistic as C -stat.

4.1. Continuum Modelling

All the spectra were initially fitted with a power law and their corresponding Galactic absorption, modelled with `Tbabs` (Wilms et al. 2000), with column densities obtained from the `HI4PI Collaboration et al. (2016)` survey. In order to accurately parameterise the properties of the underlying continuum, additional model components were required in the process such as warm or neutral absorption, or a soft excess, as outlined in Sections 4.1.1 and 4.1.2.

We note that statistically identical results could have been achieved by modelling the continuum with distant and/or ionised Compton reflection models such as `xillver` (García et al. 2013) or `relxill` (Dauser et al. 2014; García et al. 2014). Since the *XMM-Newton* bandpass is 0.3–10 keV, the contribution from the Compton reflection continuum is not well constrained, therefore, for simplicity, here we adopt a power-law plus blackbody (when required) parameterization of the continuum. A similar approach was also adopted in the *CAIXA* sample by Bianchi et al. (2009). Nonetheless, a thorough investigation using Compton and relativistic reflection models is addressed in a forthcoming companion paper, where we take advantage of the *NuSTAR* follow-up obtained in 2020 (PI: Bianchi).

Our baseline phenomenological model can be described as:

$$\text{Tbabs} \times \text{XABS} \times (\text{zbody}_1 + \text{zbody}_2 + \text{powerlaw}), \quad (1)$$

where `Tbabs` represents the absorption due to our Galaxy, `powerlaw` accounts for the primary emission component, and `zbody`_{1,2} are two layers of blackbody emission to account for the soft X-ray excess⁴. This parameterization of the soft excess is only phenomenological and hence the corresponding temperatures are not meaningful. `XABS` (when required) corresponds to a mildly ionised warm absorption component (see Section 4.1.1).

Once the best-fit of the 0.3–10 keV continuum spectra of each of the 41 observations was reached, we performed a systematic search for iron K emission and absorption profiles between 4–10 keV through the following two methods: (i) blind-line search via energy–intensity plane contours plots (Section 4.2) and (ii) extensive Monte Carlo (e.g., Protasov et al. 2002; *MC* hereafter) simulations (Section 4.4). The modelling approach of each individual spectral component is described below and the detailed continuum and absorption parameters are tabulated in Table D.1

4.1.1. Intrinsic Absorption

Neutral or lowly ionised absorption is typically constituted by a distant (\gtrsim pc scales), less ionised and denser circumnuclear material compared to UFOs, generally outflowing at velocities in the range of ~ -100 to -1000 km s⁻¹ (e.g., Kaastra et al. 2000; Kaspi et al. 2000a; Blustin et al. 2005). These absorbers are detected in the soft X-ray part of the spectrum at energies $\lesssim 2$ –3 keV and, depending on their properties, they can add a significant curvature to the spectra below 10 keV (e.g., Matzeu et al. 2016; Boller et al. 2021), and hence affect the overall continuum and line parameters in our broadband models. In the

⁴ In some SUBWAYS targets only one blackbody component is required (see Section 4.1.2), while no blackbody component is needed for the absorbed sources 2MASS J105144+3539 and 2MASS J165315+2349.

literature, the fraction of sources with reported warm absorbers is $> 60\%$ (Tombesi et al. 2013, G13).

In 2MASS J105144+3539, an intrinsic neutral absorption column of $N_{\text{H}} = 6.7 \pm 0.4 \times 10^{21} \text{ cm}^{-2}$ and two emission lines in the soft band, likely associated to collisionally ionised gas, are required. 2MASS J165315+2349 is classified as a Seyfert 2 and so requires a different model construction in the soft X-rays, with the presence of an intrinsic neutral absorber and emission arising from a distant scattered component. The continuum model differs from Equation 1 as:

$$\text{Tbabs} \times (\text{powerlaw}_{\text{scatt}} + \text{apec}_1 + \text{apec}_2 + \text{phabs} \times \text{powerlaw}_{\text{intr}}), \quad (2)$$

where $\text{apec}_{1,2}$ (Smith et al. 2001) are thermal models accounting for two regions of emitting collisionally ionised plasma and $\text{powerlaw}_{\text{scatt}}$ reproduces the distant scattered component. $\text{powerlaw}_{\text{intr}}$ accounts for the primary continuum, which is absorbed by fully covering neutral material (phabs) with a column density of $N_{\text{H}} = 2.2 \pm 0.9 \times 10^{23} \text{ cm}^{-2}$.

In this work we model the presence of fully covering mildly ionised absorption with a specifically generated xABS model from SPEX (Kaastra et al. 1996; Steenbrugge et al. 2003) converted to an XSPEC (Arnaud 1996) table⁵ (see appendix of Parker et al. 2019b). More specifically the xABS table covers the following ranges in the parameter space: column density in the range $10^{20} \leq N_{\text{H}}/\text{cm}^{-2} \leq 10^{22}$ with 10 logarithmic steps, and ionisation in the range $-4 \leq \log(\xi/\text{erg cm s}^{-1}) \leq 6$ with 20 linear steps, making this table well suited for investigating a wide range of absorbers in AGN such as warm absorbers. Although the presence of warm absorbers could have a minimal effect on the Fe K region, we find it essential to include them as the most reliable continuum level must be determined.

The xABS table was generated by assuming the default SPEX setting where the spectral energy distribution (SED) of NGC 5548 was used as representative of a standard AGN input spectrum⁶ (see Steenbrugge et al. 2005, for more details). Another parameter in the model is the 2D root mean square velocity (v_{rms}), which gives a measure of the velocity dispersion of the line profile.⁷ At the energy resolution of the EPIC CCDs (see Appendix C), the individual soft X-ray absorption lines are indeed unresolved, so in the fitting procedure the RMS velocity broadening was frozen to its default value, i.e., $v_{\text{rms}} = 100 \text{ km s}^{-1}$ (unless specified otherwise) and the systemic velocities are set to 0 km s^{-1} .

Here we also consider the possibility of partial covering along the line-of-sight. In this regime a fraction corresponding to $f_{\text{cov}} < 1$ of the total flux is indeed absorbed, while a portion $1 - f_{\text{cov}}$ leaks through the absorbing layer. This can also have a dramatic effect on the emerging continuum by imprinting a prominent spectral curvature at energies $< 10 \text{ keV}$ (e.g., Matzeu et al. 2016; Boller et al. 2021). On this basis a partial covering fraction was also added to the list of free parameters in our xABS table, i.e. $0 \leq f_{\text{cov}} \leq 1$. A more comprehensive physical analysis of low- and high-ionisation outflows is presented in a companion paper.

⁵ <https://www.michaelparker.space/xspec-models>

⁶ We are aware that our xABS table is built based on the ion balance calculated for a typical Seyfert, while our sample consists of QSOs of higher luminosity. By testing the same data with an XSTAR grid with turbulent velocity of $v_{\text{turb}} = 300 \text{ km s}^{-1}$ and a power-law SED input with a photon index of $\Gamma = 2$, we get slightly higher ionisation parameters but consistent within the errors. For this reason, we allowed ξ to explore the wide range of ionisation reported above.

⁷ <https://personal.sron.nl/~jellep/spex/manual.pdf>

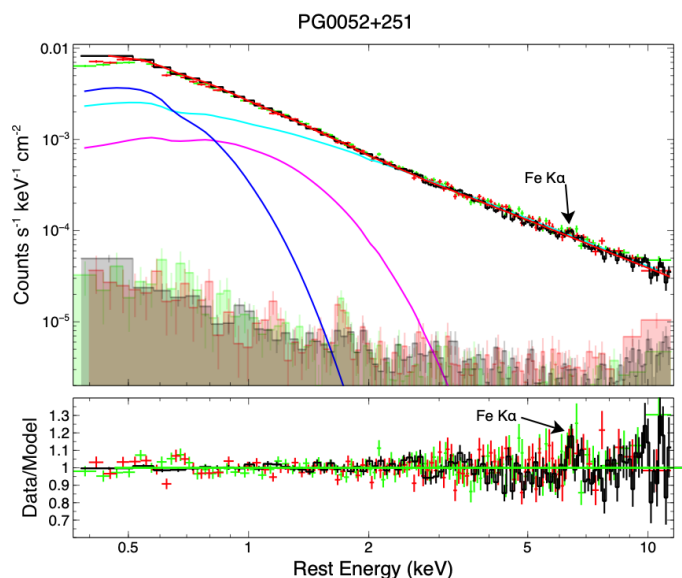


Fig. 3: Broadband EPIC data and best-fit continuum of PG 0052+251 between the rest-frame energy of 0.3–10 keV. Top: background subtracted *XMM-Newton* spectra (EPIC-pn in black, EPIC-MOS 1 in red, EPIC-MOS 2 in green) and their corresponding background levels (shaded areas). The broadband best-fit continuum model (solid red) is shown alongside the individual model components: absorbed power-law (cyan), low- (blue) and high-temperature blackbody (magenta). Bottom: corresponding residuals of the data compared to the best-fitting model.

4.1.2. The Soft Excess

The soft X-ray excess is described as a strong featureless emission component that is often observed in unabsorbed AGN below $\sim 2 \text{ keV}$. The physical mechanism responsible for this emission is still the subject of active debates, i.e. a dual-coronal system (e.g., Done et al. 2012; Petrucci et al. 2013; Rózańska et al. 2015; Middei et al. 2018; Petrucci et al. 2018; Ursini et al. 2020; Ballantyne & Xiang 2020; Porquet et al. 2021) or relativistic blurred reflection (e.g., Ross & Fabian 2005; Nardini et al. 2011; Wilkins & Fabian 2012; Walton et al. 2013; García et al. 2019; Jiang et al. 2019; Xu et al. 2021; Mallick et al. 2022)

Regardless of the physical origin of the soft excess, in this work we take a completely empirical approach by fitting its profile with one/two layers of blackbody emission, when required at the $\Delta C/\Delta \nu \gtrsim 9.3/2$ threshold (i.e., $\gtrsim 99\%$ confidence level for each blackbody component) in XSPEC (e.g., Porquet et al. 2004a; Piconcelli et al. 2005; Bianchi et al. 2009, G13). Although our phenomenological model largely ignores the detailed physics involved in the system, it allows us to fit and compare uniformly the underlying continua in our sample so that we can concentrate on the Fe K band. There might be some degeneracies between the soft excess and partial covering components during fitting, however this is not an issue for our absorption line detections. We could have modelled equally well the soft excess with a reflection component and the final result would not change, as discussed above in Section 4.1.

4.2. Search for Fe K emission and absorption

In **Figure 3** (top) we report, as an example, the background subtracted *XMM-Newton* spectra (EPIC-pn, black; EPIC-MOS 1, red; EPIC-MOS 2, green) and their corresponding background spectra of PG 0052+251. This source is one of the most luminous in the sample and is on the bright side of the luminosity/counts distribution in Type 1 AGN (see **Figure D.1**).

The 0.3–10 keV (rest-frame) best-fitting broadband continuum model (excluding iron K emission and/or absorption lines) is indicated in solid-red. The residuals are shown in the bottom panel. Our baseline continuum models include the absorbed power-law (cyan) and the two blackbody components, with high and low temperature (kT), respectively in magenta and blue. The continua are well reproduced with our baseline model (see the model statistics reported in **Table D.1**). Few exceptions were found in the sample, when the soft X-ray emission was parameterised with one or two regions of collisionally ionised plasma modelled with *apec* in 2MASS J105144+3539 and 2MASS J165315+2349, respectively. The presence of strong residuals from neutral Fe $K\alpha$ core emission at $E_{\text{rest}} = 6.4$ keV from distant material is ubiquitous in the SUBWAYS sample (e.g., see **Figure 3**).

In some observations (see **Figure D.1**) we observed strong absorption residuals (also in the Fe K band) likely associated with Fe xxv/Fe xxvi transitions. Therefore we ran a blind search, simultaneously in both EPIC-pn and EPIC-MOS spectra for every observation in the sample, in order to have a first assessment of energy, strength, shape and significance of any absorption or emission line relative to the underlying continuum model. We performed an inspection of the deviation in $|\Delta C|$ from the best-fitting continuum model by generating two-dimensional energy–intensity contours plots. This method was adopted by **T10** and **G13**, and extra details are described in **Miniutti & Fabian (2006)**.

The search was performed with our baseline continuum model (**Equation 1** or **Equation 2**) plus a narrow Gaussian line (with the velocity width fixed at $\sigma_{\text{width}} = 10$ eV). We also let the power-law photon index and normalization free to vary during the search. In adopting our broadband ‘multi-component’ continuum model above, we ensure a better reproduction accuracy of the continuum level compared to a simpler two-component power law plus Gaussian line model restricted on the Fe K band. For this routine we freeze all the soft X-rays parameters from the broadband continuum to their best-fit values, re-fit, and run the scan along with the 5–10 keV, rest frame, energy band.

The blind search method adopted here is carried out based on the following steps:

- (i) We have a baseline continuum model between 0.3–10 keV (described above) plus the unresolved Gaussian line required for the scan. The Fe $K\alpha$ emission line at 6.4 keV was not included in the baseline model. For each run, the energy of the Gaussian is scanning the three EPIC spectra simultaneously between 5–10 keV in intervals of $\Delta E = 50$ eV. The normalization of the Gaussian component probes the intensity of the spectral line and is free to vary between negative and positive values in 250 steps.
- (ii) Each individual step in the energy–intensity plane with respect to the baseline model was recorded into a file including the corresponding ΔC .
- (iii) The resulting confidence contours are plotted according to a mapped ΔC deviation of -2.3 , -4.61 , -9.21 , -13.82 and -18.52 for 2 parameters of interest corresponding to the nominal 68%, 90%, 99%, 99.9% and 99.99% confidence levels.

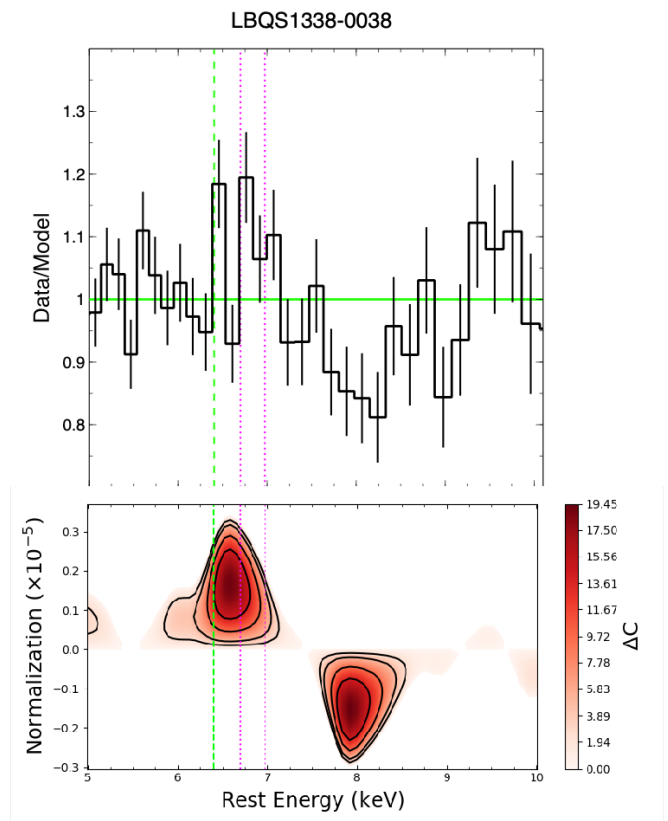


Fig. 4: Top: data/model ratio plot for the EPIC-pn spectrum (MOS 1 and MOS 2 are not included for clarity) showing the residuals in the 5–10 keV band of to the type 1 AGN LBQS 1338–0038, showing a broad emission and absorption profiles respectively at ~ 6.6 keV and ~ 8 keV suggesting a P-Cygni-like profile. The vertical lines indicate the Fe $K\alpha$ laboratory transition at $E_{\text{lab}} = 6.40$ keV (lime green) and Fe xxv and Fe xxvi at $E_{\text{lab}} = 6.70$ keV and 6.97 keV respectively (magenta). The outer to inner closed contours correspond to a ΔC significance of $(-2.3 = 68\%)$, $(-4.61 = 90\%)$, $(-9.21 = 99\%)$ and $(-13.82 = 99.9\%)$ relative to the best-fitting continuum. Bottom: Corresponding blind-search contours showing the evidence of strong emission profiles at high confidence level (see colour bar on the right).

- (iv) We inspect the contour plots to check whether there is any evidence of emission and/or absorption in the spectrum (see text below).

If an emission or absorption line is detected, it is parameterised by using a Gaussian profile. All the key Gaussian absorption and emission parameters accounting for the detected lines, using the \mathcal{KB} binning, are tabulated in **Table 2**. The ΔC mapping provided by the energy–intensity contours is a powerful tool to detect emission or absorption profiles by visually assessing the location and strength of the line relative to the underlying continuum model. The spectral complexity within the 5–10 keV band can be enhanced by a number of atomic features such as ionised emission lines from Fe xxv and Fe xxvi, at 6.7 keV and 6.97 keV respectively. As we have learned from previous work, in ultra-fast wind systems the ionised emission due to scattered photons from the outflowing material can be as important as the

absorption (e.g., Sim et al. 2008; Nardini et al. 2015; Luminari et al. 2018; Matzeu et al. 2022). In several SUBWAYS spectra, the shape of the emission and/or absorption profiles is indeed complex/broad, which suggests a superposition/blending of multiple ionised lines. Steps (i)–(iv) were carried out in each fitted EPIC spectrum of the sample.

Examples of this method are shown in Figure 4. In the top panel we show the corresponding residual of EPIC-pn spectrum (MOS 1 and MOS 2 are not included for clarity) without the emission and absorption components. The vertical dashed lines denote the position of the laboratory energy transition of Fe K α (lime green), Fe xxv (magenta) and Fe xxvi (magenta).

In Figure 4 we show the result of the same blind-search procedure applied to the type 1 AGN LBQS 1338–0038. The energy–intensity contour map is showing the presence of highly significant emission and absorption profiles at centroid rest-frame energies of $E_{\text{em}} \sim 6.6$ keV and $E_{\text{abs}} \sim 8$ keV, respectively. What differs from 2MASS J165315+2349 is that both the emission and absorption have comparable width and the emission (as well as the absorption) seems to be originating from ionised material. Such features are highly reminiscent of the well-established P-Cygni-like profile detected in PDS 456 (Nardini et al. 2015), where the emission component arises from photons scattered back into our line-of-sight from the same outflowing ionised outflow, averaged over all the viewing angles. The complete set of blind-search line contours of all the remaining observations in the sample are plotted in Appendix E, and Figure E.1. The visual inspection of the residuals makes the Fe K emission/absorption profiles detections largely qualitative at this stage. Nonetheless, we have now a strong basis to carry out a systematic identification of iron K absorption features that might be arising from an ultra-fast outflow.

4.3. Modelling the Fe K band

In this paper, we only adopt phenomenological models that are homogeneously fitted across the whole sample. All the Fe K emission and absorption residuals arising from the line blind-search (see Figure E.1) are fitted with a cosmologically redshifted Gaussian model (`zgauss` in `XSPEC`) added to equations 1 and/or 2. Modelling this way the Fe K features allows us to characterise the significance and intrinsic properties of the lines, i.e. centroid rest energy, line-width and the overall strength with respect to the underlying continuum. In some cases, when the feature is broader, we fix their line-widths (for simplicity) between $\sigma_{\text{width}} = 10$ eV–400 eV (depending on which produces a larger improvement to the fit). When the lines are broad/resolved, the line-width is left as a free parameter (see Table 2). A strong emission profile corresponding to the neutral Fe K α core at ~ 6.4 keV is present in almost every target. In some observations, of PG 0953+414, PG 1425+267, PG 1626+554, PG 1352+183, PG 1216+069, PG 0947+396_obs1, 2MASS J105144+3539 and PG 0804+761, the Fe K emission lines are more complex (see Figure E.1). Their Fe K emissions are broader and the centroid energies correspond to highly ionised iron emission in the Fe xxv and Fe xxvi domain. In the context of UFOs, broader iron K emission can arise from scattered photons from outflowing ionised material and can have crucial implications in determining the covering fraction of the outflowing gas (Sim et al. 2008, 2010; Nardini et al. 2015; Matzeu et al. 2016; Reeves & Braito 2019).

For the absorption features we estimated the outflow velocity by assuming that iron K absorption observed at energy E_{abs} is associated with H-like iron (Fe xxvi Ly α) gas, with laboratory rest-frame energy of $E_0 = 6.97$ keV. Assuming $E_0 = 6.7$ keV

(i.e. Fe xxv He α) would correspond in the above calculations to a faster v_{out} , given the larger degree of blueshift. Our choice of E_0 can be considered as a conservative choice for the outflow velocity estimate, based on the reference energy assumed. For a more appropriate identification of line transitions, i.e. either Fe xxv He α , Fe xxvi Ly α or Fe K-shell edges, we will need to carry out a photoionisation modelling of the Fe K features (with `XABS` and `XSTAR` models), which can yield an accurate description of the physical conditions of the gas, e.g. its ionisation state. A comprehensive physically motivated analysis of the emission/absorption profiles of the entire sample is the subject of a forthcoming companion paper.

For quantifying the statistical significance of the Gaussian lines in our modelling, we first adopt the ΔC improvement as used for our blind-search method. More specifically, we compute the P_F significance derived by first obtaining the $\Delta C/\Delta v$ between the best-fit with and without a specific Gaussian line and subsequently compute the F-test probability. We detected blueshifted Fe K absorption lines in 11 out of 22 sources at $P_F \gtrsim 95\%$, where 9/22 have $P_F \gtrsim 99\%$.

Numerous authors in the literature (e.g., Vaughan et al. 2003; Porquet et al. 2004b; Markowitz et al. 2006, T10; G13; Igo20, Parker et al. 2020) have established that to obtain an adequate statistical test when determining the significance of a detection of atomic lines in rather complex spectra, an extensive *MC* approach is required. In an absorption-line search framework we might detect unexpected lines at a specific energy, without any prior justification, (e.g., Protassov et al. 2002) over an arbitrary energy range. Indeed, as discussed in the next section, we find that our P_F improvements over-predict the detection probabilities, as opposed to a more robust *MC* simulation approach.

4.4. Monte Carlo approach

The *MC* simulation method has now been extensively adopted in the literature (e.g. Porquet et al. 2004b; Miniutti & Fabian 2006; Tombesi et al. 2010; Gofford et al. 2013; Nardini et al. 2019; Parker et al. 2020; Middei et al. 2020) in order to achieve a robust determination of the significance of a spectral line independently from the spectral noise and the quality of the detector. The *MC* approach overcomes the limitations of the often used F-test, which can sometimes over-predict the statistical significance of the line detection when compared to extensive *MC* simulations. In this paper the *MC* approach is focused on the Fe K absorption lines detected in 11 sources on the basis of $P_F \gtrsim 95\%$. We report the results on the detection probability based on *MC* in Table 2. This process was carried out by following these steps.

1. The continuum baseline null-hypothesis model (*NHM* hereafter) is our final best-fitting 0.3–10 keV model (see Table D.1 in Appendix D) re-adjusted after removing the Gaussian absorption component. For each test, we simulated 1000 EPIC-pn, 1000 EPIC-MOS 1 and 1000 EPIC-MOS 2 source and background spectra, by using the `fakeit` command in `XSPEC`. The simulated spectra were generated with the same exposure times and response files from the original data and grouped accordingly. We adopt the \mathcal{KB} binning (as described in Appendix C) with `FTGROUPPHA`.
2. Our 0.3–10 keV simulated spectra are then fitted with the *NHM*, which takes into account the associated uncertainties from the *NHM* itself. During this procedure, we fixed the line-width of any broad Gaussian emission features present in the spectra (both in the soft and hard X-ray band) at their corresponding best-fit energy values from the real data and we

let their intensities free to vary. The dual blackbody temperature, normalizations and any Galactic, intrinsic neutral/warm absorptions were frozen to their best-fit values of the real data reported in [Table D.1](#).

3. A narrow Gaussian profile, with line width fixed at zero, was then added to the \mathcal{NHM} , with normalization also set to zero, but free to fluctuate between negative and positive values, in order to probe both absorption and emission features. The rest-energy centroid of the Gaussian line was stepped between 5 and 10 keV in $\Delta E = 25$ eV increments with the `STEPPAR` command in `XSPEC`. Additionally, to prevent a local minimum during fitting we also enable the `SHAKEFIT` procedure developed by Simon Vaughan (see Section 3.2.2 in [Hurkett et al. 2008](#)). This process maps the ΔC variations relative to C_{null} , which are recorded after each step as $|\Delta C_{\text{noise}}|$. The degrees of freedom corresponding to both models are also recorded.
4. The above steps were repeated through $S = 1000$ iterations for each test, which produced a $|\Delta C_{\text{noise}}|$ distribution under the null-hypothesis by mapping the statistical significance of any deviations from \mathcal{NHM} due to random photon noise in the spectra.
5. The initial significance of the line derived from the real data $|\Delta C_{\text{line}}|$ was compared to the $|\Delta C_{\text{noise}}|$ distribution so that the number N of simulated spectra with a random noise fluctuation larger than the observed one can be evaluated. In case when the N simulated spectra have $|\Delta C_{\text{noise}}| \geq |\Delta C_{\text{line}}|$, the MC statistical significance (P_{MC}) of the absorption line detection can be calculated as $P_{MC} = 1 - \left(\frac{N}{S}\right)$ and reported in [Table 2](#).

In order to compare with literature results, and following e.g. [T10](#), we consider as robust detections only absorption lines with $P_F \geq 99\%$ and $P_{MC} \geq 95\%$. The discussion of the Fe K emission/absorption detection rate in our sample is presented in [Section 5.1](#).

Table 2: Gaussian emission and absorption parameters in the Fe K band corresponding to a total of 41 observations. Notes: (1) Source name; (2) observation ID; (3) measured Gaussian emission line energy in the rest-frame; (4) emission line energy width. The absorption lines were fitted with widths ranging between $\sigma_{\text{width}} 10 \text{ eV} - 400 \text{ eV}$; (5) emission line intensity in units of $\text{ph cm}^{-2} \text{ s}^{-1}$; (6) equivalent width; (7) change in C -stat fit statistic, degrees of freedom and the corresponding significance (in per cent) when the emission line is removed from the best fit. (8)–(11) same as (3)–(6) but for the Gaussian absorption line; (12) corresponding outflow velocity inferred from the rest-frame energy of the absorption line with $E_{\text{rest}} = 6.97 \text{ keV}$ as a reference energy; (13) same as (7); (14) MC significance of the absorption line where the $\geq 95\%$ values are highlighted in bold. † In this observation the absorption profile is likely arising from a blend of a Fe xxv–xxvi pair, which could be resolved by binning the spectra with `grpmin1` (see Appendix C). ‡ as the two absorption lines are consistent with a Fe xxv–xxvi pair, we inferred the null probability of both profiles simultaneously as a false detection by multiplying the probabilities of each line. ★ In this P-Cygni-like profile the line-width of the emission is tied to that of the absorption as $\sigma_{\text{em}} = (\sigma_{\text{abs}}/E_{\text{abs}}) \times E_{\text{em}}$. ^f denotes a fixed parameter during fitting. ♦ A Monte Carlo test was not applied for this feature as it is likely associated with a neutral Fe K edge.

Source (1)	Emission Lines						Absorption Lines						
	<i>XMM</i> (2) ObsID	E_{em} (3) keV	σ_{width} (4) eV	Int (5) 10^{-6}	EW (6) eV	$\Delta C/\Delta\nu(P_F)$ (7)	E_{abs} (8) keV	σ_{width} (9) eV	Int (10) 10^{-6}	EW (11) eV	v_{Gau} (12) c	$\Delta C/\Delta\nu(P_F)$ (13)	P_{MC} (14)
PG0052+251	0841480101	$6.40_{-0.06}^{+0.06}$	10^f	$3.3_{-1.5}^{+1.5}$	33_{-15}^{+15}	16.3/2 (> 99.9%)							
PG0953+414	0841480201	$6.42_{-0.06}^{+0.06}$ $6.92_{-0.08}^{+0.07}$	10^f 100^t	$1.9_{-1.0}^{+1.0}$ $3.2_{-1.0}^{+1.1}$	36_{-20}^{+20} 73_{-23}^{+26}	11.95/2 (99.75%) 24.87/2 (> 99.99%)	$7.82_{-0.10}^{+0.10}$	10^f	$-1.5_{-0.8}^{+0.9}$	-43_{-24}^{+24}	$-0.116_{-0.012}^{+0.012}$	8.56/2 (98.62%)	82.1%
PG1626+554	0841480401	$6.40_{-0.07}^{+0.08}$ $7.01_{-0.15}^{+0.12}$	100^f 100^f	$2.6_{-0.9}^{+0.9}$ $2.1_{-1.1}^{+1.1}$	63_{-22}^{+22} 60_{-36}^{+36}	21.02/2 (> 99.99%) 9.87/2 (99.28%)							
PG1202+281	0841480501	$6.45_{-0.05}^{+0.05}$ $7.09_{-0.08}^{+0.09}$	10^f 10^f	$2.1_{-1.0}^{+1.0}$ $1.67_{-1.0}^{+1.0}$	37_{-18}^{+18} 34_{-21}^{+21}	13.7/2 (99.89%) 8.0/2 (98.17%)	$7.78_{-0.06}^{+0.06}$	10^f	$-1.9_{-0.9}^{+0.9}$	-45_{-21}^{+21}	$-0.113_{-0.012}^{+0.012}$	10.3/2 (99.42%)	95.0%
PG1435–067	0841480601	$6.37_{-0.06}^{+0.06}$	10^f	$1.8_{-0.74}^{+0.78}$	100_{-36}^{+39}	19.0/2 (> 99.99%)	$8.28_{-0.45}^{+0.70}$	400^f	$-2.2_{-1.4}^{+1.4}$	-184_{-117}^{+117}	$-0.166_{-0.053}^{+0.079}$	9.52/2 (99.14%)	90.9%
SDSS J144414+0633	0841480701	$6.43_{-0.03}^{+0.03}$	10^f	$2.8_{-0.8}^{+0.8}$	64_{-18}^{+18}	37.48/2 (> 99.99%)							
2MASS J165315+2349†	0841480801	$6.37_{-0.03}^{+0.03}$ $8.87_{-0.17}^{+0.13}$	10^f 100^f	$3.4_{-0.9}^{+0.9}$ $2.5_{-1.3}^{+1.3}$	73_{-20}^{+20} 87_{-39}^{+43}	49.09/2 (> 99.99%) 10.48/2 (99.64%)	$7.42_{-0.06}^{+0.06}$ $7.77_{-0.07}^{+0.06}$	10^f 10^f	$-1.8_{-0.8}^{+0.8}$ $-1.8_{-0.8}^{+0.9}$	-48_{-21}^{+21} -56_{-25}^{+28}	$-0.082_{-0.012}^{+0.012}$ $-0.108_{-0.010}^{+0.009}$	14.39/2 (> 99.9%) 14.97/2 (> 99.9%)	> 99.9% ‡
PG1216+069	0841480901	$6.47_{-0.13}^{+0.12}$	182_{-129}^{+181}	$2.8_{-1.2}^{+1.5}$	68_{-29}^{+36}	21.28/3 (> 99.99%)							
PG0947+396 (Obs 1)	0841481001	$6.43_{-0.06}^{+0.06}$ $6.96_{-0.11}^{+0.12}$	10^f 10^f	$2.2_{-1.0}^{+1.0}$ $1.4_{-0.9}^{+1.0}$	88_{-31}^{+31} 64_{-45}^{+45}	23.8/2 (> 99.99%) 9.47/2 (99.12%)	$9.51_{-0.11}^{+0.10}$	10^f	$-2.2_{-0.9}^{+1.0}$	-169_{-69}^{+77}	$-0.300_{-0.010}^{+0.010}$	11.65/2 (99.7%)	96.9%
PG0947+396 (Obs 2)	0841482301	$6.35_{-0.06}^{+0.06}$	100^f	$3.0_{-0.9}^{+0.9}$	132_{-40}^{+40}	35.02/2 (> 99.99%)							
WISE J053756–0245	0841481101	$6.40_{-0.06}^{+0.06}$	10^f	$1.5_{-0.6}^{+0.6}$	81_{-32}^{+32}	21.0/2 (> 99.99%)							
HB 891529+050	0841481301	$6.47_{-0.04}^{+0.04}$	10^f	$2.0_{-0.5}^{+0.5}$	103_{-26}^{+26}	38.88/2 (> 99.99%)							
PG1307+085	0841481401	$6.35_{-0.06}^{+0.06}$	100^f	$3.5_{-1.0}^{+1.0}$	64_{-18}^{+18}	35.74/2 (> 99.99%)							
PG1425+267	0841481501	$6.40_{-0.03}^{+0.03}$ $6.88_{-0.06}^{+0.06}$	10^f 10^f	$3.0_{-0.7}^{+0.7}$ $1.4_{-0.7}^{+0.7}$	73_{-17}^{+17} 38_{-20}^{+20}	48.12/2 (> 99.99%) 11.91/2 (98.74%)	$8.24_{-0.06}^{+0.06}$	10^f	$-1.2_{-0.6}^{+0.6}$	-46_{-24}^{+23}	$-0.166_{-0.009}^{+0.009}$	10.09/2 (99.36%)	93.2%
PG1352+183	0841481601	$6.53_{-0.12}^{+0.13}$	468_{-113}^{+138}	$6.0_{-1.6}^{+1.8}$	319_{-83}^{+96}	74.69/3 (> 99.99%)							
2MASS J105144+3539	0841481701	$6.37_{-0.08}^{+0.08}$	100^f	$1.7_{-0.5}^{+0.5}$	156_{-56}^{+75}	35.66/3 (> 99.99%)	$8.51_{-0.07}^{+0.08}$	100^f	$-0.78_{-0.33}^{+0.38}$	-108_{-46}^{+52}	$-0.197_{-0.009}^{+0.009}$	10.56/2 (99.49%)	95.9%
2MASS J0220–0728	0841481901	$6.39_{-0.06}^{+0.05}$	10^f	$1.3_{-0.5}^{+0.5}$	60_{-23}^{+23}	15.58/2 (> 99.9%)							
LBQS 1338–0038	0841482101	$6.62_{-0.21}^{+0.94}$	311_{-124}^{+432}	$2.5_{-1.3}^{+1.1}$	67_{-35}^{+}	15.09/2 (> 99.99%)	$8.03_{-1.06}^{+0.20}$ $11.06_{-0.29}^{+0.29}$	378^* 378^f	$-3.6_{-1.1}^{+1.1}$ $-3.01_{-1.3}^{+1.3}$	-130_{-41}^{+41} -187_{-81}^{+81}	$-0.139_{-0.02}^{+0.02}$ $-0.432_{-0.041}^{+0.041}$	24.14/3 (> 99.9%) 10.00/2 (99.33%)	> 99.9% 87.2%

Source (1)	XMM (2) ObsID	E_{em} (3) keV	σ_{width} (4) eV	Emission Lines			Absorption Lines						
				Int (5) 10^{-6}	EW (6) eV	$\Delta C/\Delta v (P_F)$ (7)	E_{abs} (8) keV	σ_{width} (9) eV	Int (10) 10^{-6}	EW (11) eV	v_{Gau} (12) c	$\Delta C/\Delta v (P_F)$ (13)	P_{MC} (14)
PG0804+761	0102040401	$6.33^{+0.08}_{-0.07}$	10^f	$8.2^{+5.4}_{-5.1}$	60^{+40}_{-37}	7.43/2 (97.56%)	$7.93^{+0.06}_{-0.06}$	10^f	$-11.7^{+4.6}_{-4.2}$	-133^{+52}_{-48}	$-0.128^{+0.007}_{-0.006}$	15.99/2 (> 99.99%)	99.8%
		$6.96^{+0.16}_{-0.17}$	10^f	$8.4^{+5.7}_{-5.3}$	74^{+50}_{-47}	7.50/2 (97.65%)							
	0605110101	$6.41^{+0.08}_{-0.07}$	100^f	$8.0^{+2.8}_{-2.8}$	69^{+24}_{-24}	25.77/2 (> 99.99%)							
		$6.81^{+0.16}_{-0.17}$	10^f	$4.7^{+2.3}_{-2.2}$	44^{+22}_{-21}	13.89/2 (> 99.99%)							
	0605110201	$6.58^{+0.09}_{-0.09}$	388^{+104}_{-80}	$26.4^{+6.5}_{-5.7}$	328^{+81}_{-71}	115.0/3 (> 99.99%)							
PG1416-129	0203770201	$6.36^{+0.04}_{-0.05}$	10^f	$3.0^{+1.1}_{-1.1}$	61^{+22}_{-22}	22.13/2 (> 99.99%)							
PG1402+261	0400200101	$6.37^{+0.07}_{-0.07}$	10^f	$1.9^{+1.0}_{-1.0}$	82^{+55}_{-49}	10.88/2 (99.57%)							
		$7.40^{+0.09}_{-0.10}$	10^f	$1.5^{+1.0}_{-0.9}$	76^{+40}_{-40}	7.42/2 (97.55%)							
	0830470101	$6.15^{+0.15}_{-0.16}$	100^f	$1.1^{+0.7}_{-0.7}$	42^{+27}_{-27}	11.69/2 (99.71%)							
		$8.36^{+0.06}_{-0.06}$	10^f	$0.86^{+0.74}_{-0.72}$	67^{+58}_{-56}	7.74/2 (97.91%)							
HB89 1257+286	0204040101	$6.34^{+0.04}_{-0.05}$	100^f	$2.2^{+0.6}_{-0.6}$	85^{+23}_{-23}	38.3/2 (> 99.99%)	$8.78^{+0.15}_{-0.16}$	10^f	$-1.1^{+0.7}_{-0.7}$	-81^{+54}_{-54}	$-0.227^{+0.016}_{-0.018}$	6.33/2 (95.78%)	65.8%
	0204040201	$6.37^{+0.04}_{-0.05}$	10^f	$1.5^{+0.5}_{-0.5}$	93^{+31}_{-31}	27.2/2 (> 99.99%)							
	0204040301	$6.35^{+0.09}_{-0.08}$	100^f	$1.7^{+0.7}_{-0.7}$	82^{+34}_{-34}	18.9/2 (> 99.99%)							
		$6.93^{+0.09}_{-0.09}$	100^f	$1.5^{+0.7}_{-0.7}$	84^{+38}_{-38}	14.5/2 (98.74%)							
	0304320201	$6.46^{+0.15}_{-0.13}$	284^{+213}_{-200}	$4.7^{+1.8}_{-1.5}$	156^{+60}_{-50}	27.2/3 (> 99.99%)							
	0304320301	$6.49^{+0.08}_{-0.08}$	10^f	$1.2^{+0.7}_{-0.7}$	66^{+39}_{-39}	9.7/2 (99.23%)							
	0304320801	$6.41^{+0.13}_{-0.13}$	10^f	$1.1^{+0.8}_{-0.8}$	44^{+32}_{-32}	6.36/2 (95.84%)							
		0109080801	$6.56^{+0.07}_{-0.07}$	200^{+57}_{-47}	$11.2^{+2.3}_{-2.2}$	279^{+57}_{-55}	103.9/2 (> 99.99%)						
PG 1114+445	0651330101	$6.48^{+0.06}_{-0.06}$	143^{+74}_{-56}	$8.3^{+2.4}_{-2.2}$	230^{+67}_{-61}	54.9/2 (> 99.99%)	$7.49^{+0.29}_{-0.28}$	300^f	$-4.2^{+2.0}_{-1.9}$	-158^{+75}_{-71}	$-0.072^{+0.042}_{-0.042}$	11.71/2 (99.7%)	95.5%
	0651330301	$6.42^{+0.05}_{-0.05}$	50^f	$4.4^{+1.6}_{-1.4}$	133^{+43}_{-40}	29.2/2 (> 99.99%)	$7.35^{+0.12}_{-0.19}$	100^f	$-2.6^{+1.2}_{-1.1}$	-94^{+38}_{-35}	$-0.053^{+0.017}_{-0.027}$	11.9/2 (99.7%)	97.2%
	0651330401	$6.48^{+0.06}_{-0.07}$	170^{+75}_{-55}	$10.6^{+4.4}_{-3.2}$	261^{+108}_{-79}	56.9/3 (> 99.99%)	$7.21^{+0.11}_{-0.14}$	10^f	$-2.1^{+1.4}_{-1.3}$	-68^{+45}_{-42}	$-0.034^{+0.020}_{-0.015}$	8.3/2 (98.4%)	90.5%
	0651330501	$6.42^{+0.05}_{-0.04}$	10^f	$6.9^{+2.1}_{-1.9}$	178^{+54}_{-49}	49.6/2 (> 99.99%)	$7.04^{+0.12}_{-0.08}$	10^f	$-2.7^{+1.4}_{-1.3}$	-79^{+41}_{-38}	-	10.02/2 (99.33%)	(N/A)♦
	0651330601	$6.51^{+0.05}_{-0.09}$	100^f	$8.5^{+4.7}_{-4.2}$	121^{+67}_{-60}	32.3/2 (> 99.99%)							
	0651330701	$6.49^{+0.04}_{-0.04}$	50^f	$6.6^{+2.6}_{-2.3}$	117^{+46}_{-41}	29.4/2 (> 99.99%)							
	0651330801	$6.42^{+0.09}_{-0.09}$	100^f	$5.3^{+1.2}_{-2.1}$	126^{+29}_{-50}	21.6/2 (> 99.99%)							
		$9.02^{+0.16}_{-0.17}$	227^{+177}_{-156}	$5.7^{+3.6}_{-3.0}$	266^{+168}_{-140}	12.9/3 (99.51%)							
	0651330901	$6.44^{+0.06}_{-0.07}$	50^f	$4.4^{+2.2}_{-1.7}$	96^{+46}_{-37}	21.5/2 (> 99.99%)							
	0651331001	$6.50^{+0.05}_{-0.06}$	134^{+67}_{-64}	$8.6^{+2.8}_{-2.4}$	214^{+70}_{-60}	48.8/3 (> 99.99%)							
0651331101	$6.42^{+0.09}_{-0.09}$	50^f	$4.3^{+2.6}_{-2.0}$	92^{+66}_{-43}	13.1/2 (99.86%)								

5. Results

A total of 14 absorption features with energies $E_{\text{rest}} \gtrsim 7.1$ keV and $P_F \gtrsim 99\%$ are found. Of these, 8 are robustly detected with $P_{MC} \gtrsim 95\%$ while 6 have $P_{MC} < 95\%$ and are therefore considered non-detections. In PG 1114+445 (ObsID 0651330501) an absorption line at $E_{\text{rest}} = 7.04^{+0.12}_{-0.08}$ keV was detected at the $P_F > 99\%$ confidence level. However, such a feature is likely consistent with a neutral iron K edge so no Monte Carlo test was applied here.

In Figure 5 (top), we plot the unfolded EPIC-pn (black), MOS 1 (red) and 2 (green) data showing the 8 Fe K absorption lines detections with $P_{MC} \gtrsim 95\%$. To avoid model and data convolution issues, the spectra in each panel are initially unfolded against a simple $\Gamma = 2$ power law (with normalisation of 1) and subsequently their corresponding best-fitting model are superimposed (solid red). In Figure 5 (middle) the plot is in terms of the EPIC data counts normalised by the effective areas and Figure 5 (bottom) are their corresponding residuals.

We conservatively identify these Fe K absorption lines as highly ionised iron, specifically Fe xxv Ly α K-shell transitions, all blueshifted with respect to their laboratory rest energies. Some of these lines can be a blend of both Fe xxv He α and Fe xxv Ly α resonant transitions and might be indistinguishable with the current EPIC energy resolution. In a forthcoming paper (Matzeu et al., in preparation), we will carry out a comprehensive physical modelling of these features where an accurate measurement of the ionisation balance, as well as density and velocity, of the outflowing gas can be achieved. A photoionisation analysis of the Fe K lines will also help towards a quantitative identification of the absorption/emission features. As presented in Section 4.3, the corresponding outflow velocities were conservatively estimated by choosing $E_{\text{rest}} = 6.97$ keV as a reference energy (see Table 2).

5.1. Line Detection Rate

Here, we quantify the probability of whether or not the detected absorption lines are caused by statistical fluctuation (‘shot noise’). This can be done by using the binomial distribution (e.g., T10; G13). For an event with a null-probability p , the likelihood of n detections after N trials is given by the expression:

$$P(n; N, p) = \frac{N!}{n!(N-n)!} p^n (1-p)^{N-n}. \quad (3)$$

In this context, n is the number of absorption lines detected in N systems and depending on the latter quantity we investigate two different cases where we take into account: case (i) all the individual targets, or $N_{(i)} = 22$; and case (ii) all the individual observations (with total net counts of ≥ 1500 cts in the 4–10 keV band), or $N_{(ii)} = 41$.

In case (i) we have $n_{95} = 7$ Fe K absorption line systems detected in $N_{(i)} = 22$ observations at a significance of $P_{MC} \geq 95\%$. So the probability of one of these absorption profiles being due to fluctuating noise can be taken as $p < 0.05$. The probability of all of the observed absorption systems being associated with noise is then reasonably low, with $P_{95,(i)} < 6.17 \times 10^{-5}$ ($\lesssim 0.006\%$). This suggests that the observed lines are unlikely to be associated with simple statistical fluctuations in the spectra.

In case (ii) we have a total of $n_{95} = 8$ detections out of $N_{(ii)} = 41$ individual observations. Here we have $P_{95,(ii)} < 6.89 \times 10^{-4}$ ($\lesssim 0.07\%$).

5.2. Photoionisation modelling of Fe K features: initial results

Although this paper is solely focused on UFO detection, we present a preliminary photoionization analysis of the Fe K features and we provide first-order physical measurements of their properties. This analysis is carried out so that our SUBWAYS results can be compared with those previously obtained in Tombesi et al. (2011, T11 hereafter) T11, G13 and Igo20. The search for absorption features and the Gaussian modelling of the absorption profiles in the Fe K band described in Section 4.3 suggest they can be ascribed to outflowing and highly ionised material likely associated with Fe xxv He α –Fe xxv Ly α transitions.

In contrast with the phenomenological models used before, modelling the absorption features with xSTAR allows us to probe the physical properties of the absorbing medium. More specifically we are able to quantify the ionization state (ξ), the column density (N_H) and the systemic redshift of the material relative to the observed one, which translates into the outflow velocity (v_{out} ; see below for more details). Through the photoionization modelling approach it is also possible to infer the geometric properties, such as the radial distance from the ionizing source, the covering factor and the resulting overall kinematics (e.g., Gofford et al. 2015; Matzeu et al. 2017).

We replaced the Gaussian absorption profiles, detected at the $P_{MC} \gtrsim 95\%$ confidence level, with xSTAR photoionization models, generated with a power-law SED input spectrum of $\Gamma = 2$, by using the xSTAR suite v2.54a (Bautista & Kallman 2001; Kallman et al. 2004). We adopted various xSTAR grids with different turbulent velocity, defined as $\sigma_{\text{turb}} = \sqrt{2}\sigma$, so that an accurate description of the width of the Fe K absorption lines could be provided. Choosing a grid with a smaller σ_{turb} results in a smaller equivalent width of the profile in the data, and the absorption would saturate too quickly at lower N_H . So for each source we adopted grids with σ_{turb} ranging between 1000–10000 km s $^{-1}$ (see Table 3).

The measured column densities are ranging between $10^{23} \lesssim N_H/\text{cm}^{-2} \lesssim 10^{24}$ with a mean value of $\log(N_H/\text{cm}^{-2}) \sim 23.6$ and a median of $\log(N_H/\text{cm}^{-2}) \sim 23.8$. We also report the measured ionization distribution, which is found to extend between $3.5 \lesssim \log(\xi/\text{erg cm s}^{-1}) \lesssim 5.5$, with mean/median values of $\log(\bar{\xi}/\text{erg cm s}^{-1}) \sim 4.7$ and $\log(\tilde{\xi}/\text{erg cm s}^{-1}) \sim 4.8$, respectively.

The outflow velocity distribution measured with xSTAR⁸ ranges between $-0.3 \lesssim v_{\text{out}}/c \lesssim -0.1$ (see Table 3). The mean/median values are $\bar{v}_{\text{out}} \sim -0.144c$ and $\tilde{v}_{\text{out}} \sim -0.110c$ respectively. We also compare the outflow velocities measured with xSTAR and with the one measured from the Gaussian fitting. For the latter, the measured velocities are found to lie between $-0.3 \lesssim v_{\text{out}}/c \lesssim -0.05$ (see Table 2) with mean/median values of $\bar{v}_{\text{out,Gauss}} \sim -0.131c$ and $\tilde{v}_{\text{out,Gauss}} \sim -0.113c$ respectively. We find that both the phenomenological and the physical modelling of the Fe K absorption features have the same distribution, as confirmed at the 99.7% confidence level by a Kolmogorov-Smirnov test. The xSTAR-based approach returns a $\sim 10\%$ higher mean velocity but a comparable median, within $\sim 3\%$.

In our sample a considerable fraction of the Fe K absorbers are characterised by material with high column density and highly ionised material, likely H-like iron. Such result does not come as surprise when considering the hard average photon-index ($\bar{\Gamma} \sim$

⁸ The systemic redshift of the absorber obtained from fitting with xSTAR is given in the observer’s rest-frame z_{abs} and related to $v_{z_{\text{abs}}} = \left[(1 + z_{\text{abs}})^2 - 1 \right] / \left[(1 + z_{\text{abs}})^2 + 1 \right]$, and correcting for the systemic velocities of the sources u we obtain $v_{\text{out}}/c = (u - v_{z_{\text{abs}}}) / \left[1 - (uv_{z_{\text{abs}}}) \right]$.

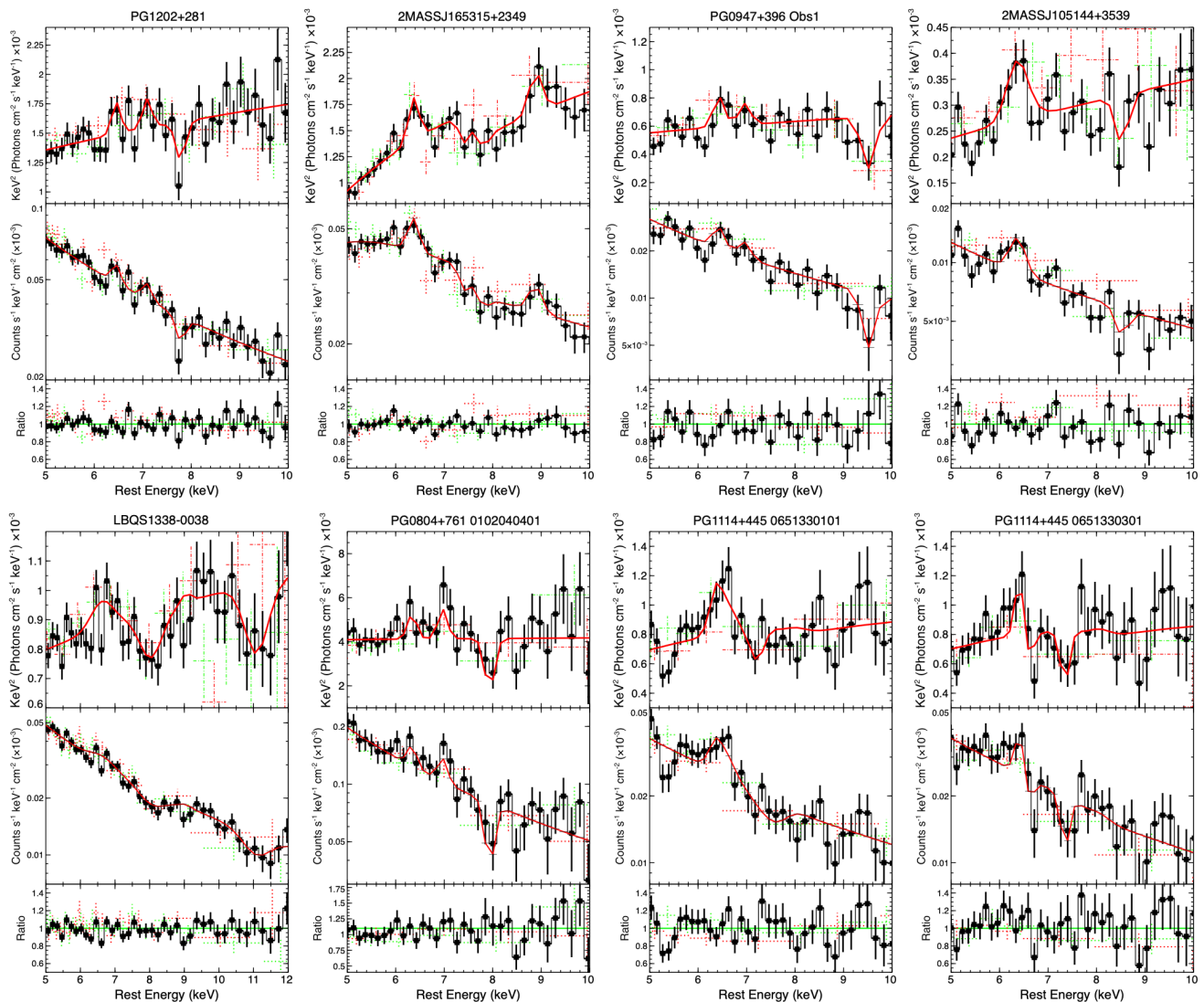


Fig. 5: Top: Unfolded EPIC-pn (black), EPIC-MOS 1 (dashed red) and EPIC-MOS 2 (dashed green) spectra, between 5–10 keV, of the 8 observations where the Fe K absorption line was detected at $P_{MC} \gtrsim 95\%$. The spectra were firstly unfolded against a power law of $\Gamma = 2$ and their corresponding best-fitting model (solid red) overlaid on top afterwards. Middle: Corresponding EPIC data counts and best-fitting model. Bottom: Data/Model ratio. The presumed absorption features at ~ 9.2 keV and ~ 9.5 keV present in e.g., 2MASSJ105144+3539 and 2MASS J165315+2349, respectively, are simply not significant enough to be considered as detections (see Figure 4 and Figure E.1), and hence they were not included in the best-fitting models.

1.8) measured on the entire sample (see Figure 6), which would overionise the outflowing material (see Matzeu et al. 2022, Figs. 2 and 3). A comprehensive photoionisation analysis with *xSTAR* (and other physically motivated wind models) will be presented in a companion paper, where customised photoionization tables will be generated with more realistic optical/UV/X-ray SED inputs for each individual SUBWAYS source (e.g., Nardini et al. 2015; Matzeu et al. 2016).

6. Discussion

In this work, we searched for Fe K absorption features in a sample of 22 targets (41 observations), of which 17 were observed as part of the *XMM-Newton* large program carried out in AO18. Through a systematic blind line scan performed in all the observations and supported by a MC procedure, we detected iron K absorption lines in 7/22 sources (i.e., $\sim 30\%$) at the $P_{MC} \gtrsim 95\%$ confidence level. Through our statistical approach, we have

found 2 robust Fe K absorption line detections at $P_{MC} \gtrsim 99\%$ in 2MASS J165315+2349 and LBQS 1338–0038. The remaining 5 detections are still significant but with $95\% \leq P_{MC} \leq 99\%$, in PG 1202+281, 2MASS J105144+3539, PG 1114+445, PG 0804+761 and PG 0947+396 (see Table 2).

Such absorption (and sometimes emission) profiles are associated with highly ionised He- and/or H-like iron, arising from the outflowing material, as their centroid energy is blueshifted with respect to the QSO systemic redshift. In this paper we only focused on the search and phenomenological analysis of such features, thus for the estimate of the outflow velocities we assumed $\text{FeXXVI Ly}\alpha$ at $E_{\text{rest}} = 6.97$ keV as a reference energy for a conservative result, which correspond to the lowest possible outflow velocity. Accordingly, we found that the average outflow velocity measured in our sample is $\bar{v}_{\text{out}} = -0.133c$, as shown in Figure 7.

Table 3: x_{STAR} parameters for the Fe K absorption features detected in the SUBWAYS sample with $P_{\text{MC}} \gtrsim 95\%$. Notes: (1) Source name; (2) observation ID; (3) intrinsic velocity broadening of the x_{STAR} grid; (4) column density and (5) gas ionisation state both in log scale; (6) change in C -stat fit statistic over degrees of freedoms when x_{STAR} is removed; (7) corresponding significance in per cent.

Source (1)	ObsID (2)	x_{STAR} parameters					
		σ_{turb} (3) km s ⁻¹	$\log(N_{\text{H}})$ (4) cm ⁻²	$\log(\xi)$ (5) erg cm s ⁻¹	v_{out} (6) c	$\Delta C/\Delta \nu$ (7)	(P_{F}) (8)
PG1202+281	0841480501	1000	> 23.84	> 5.02	$-0.108^{+0.010}_{-0.08}$	8.60/3	96.49%
2MASS J165315+2349 [†]	0841480801	5000	$23.76^{+0.39}_{-0.15}$	$4.76^{+0.59}_{-0.42}$	$-0.110^{+0.008}_{-0.015}$	-22.98/3	> 99.99%
PG0947+396 (Obs 1)	0841481001	5000	> 23.68	$5.38^{+0.44}_{-1.27}$	$-0.305^{+0.037}_{-0.019}$	10.8/3	98.71%
2MASS J105144+3539	0841481701	1000	$22.78^{+0.67}_{-0.33}$	$4.10^{+0.35}_{-0.38}$	$-0.237^{+0.011}_{-0.010}$	10.9/3	98.77%
LBQS 1338-0038	0841482101	10000	$23.16^{+1.01}_{-0.22}$	$5.01^{+0.64}_{-0.38}$	$-0.152^{+0.020}_{-0.023}$	23.27/3	> 99.99%
PG0804+761	0102040401	5000	$23.93^{+0.33}_{-0.27}$	> 4.49	$-0.130^{+0.011}_{-0.011}$	11.1/3	98.88%
PG1114+445	0651330101	5000	$23.90^{+0.25}_{-0.16}$	$4.65^{+0.77}_{-0.44}$	$-0.072^{+0.017}_{-0.016}$	11.91/3	99.23%
	0651330301	5000	$23.61^{+0.10}_{-0.15}$	$3.56^{+0.10}_{-0.13}$	$-0.070^{+0.017}_{-0.015}$	62.08/3	> 99.99%

For our search of Fe K absorption and emission features, an accurate parameterization of the underlying broadband continuum (i.e., 0.3–10 keV) in each observation was required. We therefore summarise the phenomenological continuum findings of SUBWAYS. We found that 27 out of the 41 (~ 65%) SUBWAYS observations are characterised by intrinsic soft X-ray absorption. More specifically, 20/27 systems can be identified as fully covering, mildly ionised (warm) absorbers, while 5/27 are partially covering the line-of-sight. We note that 2/27 spectra are modified by a fully covering neutral absorber, where in 2MASS J165315+2349 the spectral curvature at energies < 2 keV is caused by a column density $N_{\text{H}} \sim 10^{23} \text{ cm}^{-2}$, consistent with the values measured in Seyfert 2 galaxies. We find that a prominent soft excess, at a > 99% significance, is present in the majority of the spectra in our sample, i.e. 39/41, where one zbody component is required in 13/39 and two components in 26/39 sources.

In Figure 6 we compare the primary continuum photon indices (Γ) with those measured in previous works in the literature: a purely X-ray selected sample, CAIXA (Bianchi et al. 2009), an optically selected PG QSO sample (Piconcelli et al. 2005), low- z AGN analyzed with *XMM-Newton* (T10) and *Suzaku* (G13). We find that the SUBWAYS sample tends to be characterised by $\Gamma < 2$ ($\bar{\Gamma} = 1.81$), only slightly harder compared to the optically selected PG QSO sample ($\bar{\Gamma} = 1.89$) and largely consistent with the CAIXA (Bianchi et al. 2009) ($\bar{\Gamma} = 1.78$) and T10 ($\bar{\Gamma} = 1.77$) samples. The mean photon index of the *Suzaku* sample is softer, with ($\bar{\Gamma} = 1.95$).

6.1. Sample comparisons

The SUBWAYS sample size is indeed small compared to those in T10; G13 and Igo20. With this in mind this selection of tar-

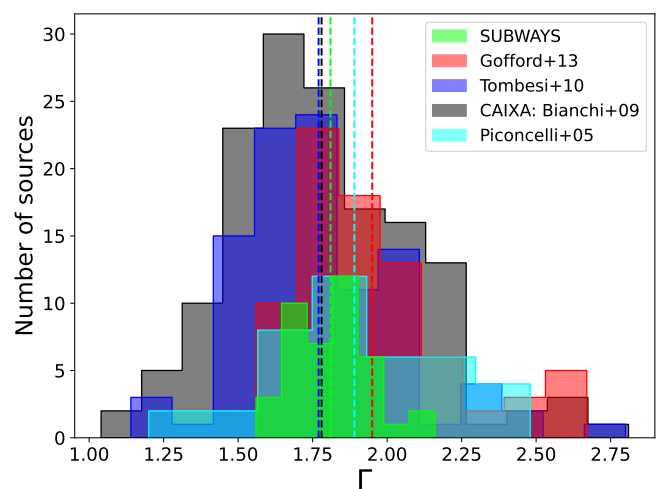


Fig. 6: Histogram comparing the photon-index (Γ) measured in SUBWAYS (green), this work, with mean value of $\bar{\Gamma} = 1.81$ (vertical line), with those measured in an X-ray selected sample (CAIXA sample, 150 sources with $\bar{\Gamma} = 1.78$; Bianchi et al. 2009); PG QSO sample (Piconcelli et al. 2005, 40 sources $\bar{\Gamma} = 1.89$); local AGN (T10; G13 with $\bar{\Gamma} = 1.77$ and $\bar{\Gamma} = 1.95$ respectively).

gets must be taken as an initial exploration of the intermediate- z population that is bridging the gap of UFOs studies between low- and high- z sources.

We find that our overall measurements seem to be skewed to higher values of N_{H} and v_{out} compared to T10 and G13,

whilst the ionization state of the absorber is on the same order of magnitude (slightly lower). The latter parameter can be influenced by the SED input assumed when generating the photoionization grids. We also find that the outflow velocity measured in PG0947+396 (Obs1), being the highest in the sample, is unlikely to be associated with outflowing, highly ionised material, but rather the result of an artefact of the EPIC CCD or/and some background issue. Although the absorption line is significantly detected at the $P_F > 99\%$ (Gaussian modelling) and $P_{MC} \sim 97\%$ (Monte Carlo approach) confidence level, it is weakly detected with *XSTAR* at $\sim 90\%$. Furthermore, an outflow velocity of $v_{out} > 0.30c$ is generally considered on the high end of the scale of ultra fast winds and can carry a huge amount of kinetic power (e.g., Matzeu et al. 2017; Reeves et al. 2018a). These events are more likely to be present in highly accreting sources where $L_{bol}/L_{Edd} \rightarrow 1$ (or above) and Eddington fractions of $L_{bol}/L_{Edd} \sim 10\%$ (Bianchi et al. 2009) might be not enough to drive such strong outflows, although it cannot be ruled out as magneto-hydrodynamic (MHD) driving mechanisms could come into play (e.g. Fukumura et al. 2010; Kraemer et al. 2018; Luminari et al. 2021; Fukumura et al. 2022), especially in low-Eddington regimes.

In Figure 7, we show the v_{out} distributions, and their mean values, measured with *XMM-Newton* in previous works in the literature, such as in T10, $\bar{v}_{out} = -0.109c$; Igo20, $\bar{v}_{out} = -0.138c$; C21, $\bar{v}_{out} = -0.330c$. An interesting trend is shown in Figure 7. By looking at all the measurements, the UFO outflow velocities seem to increase with redshift. Although the statistical footing of this trend is beyond the scope of this paper, we can recognise that such behaviour does arise from a high- L_{bol} selection bias expected in sources at progressively higher redshift as the feeding becomes stronger (e.g., Di Matteo et al. 2005), in particular due to the larger inflow of cold gas mass triggering CCA and boosting accretion rates by a few orders of magnitude compared with quiescent hot modes (e.g., Gaspari et al. 2017). Another way to interpret this trend is simply realise that the outflow velocity seems to increase with the luminosity (e.g., Saez & Chartas 2011; Matzeu et al. 2017; Chartas & Canas 2018, C21), as shown below in Figure 8, and on the other hand the most luminous sources are observed at higher z . Additionally, another possible bias that is involved at higher z is that higher velocity shifts become more detectable with increasing redshift.

In Figure 8 we show the wind velocities, as measured from our X-ray spectral fits with Gaussian lines and tabulated in Table 2, plotted against the bolometric luminosity of the SUBWAYS targets (see Table 1) shown as red stars. We added and recomputed the fit of the correlation of v_{wind} versus L_{bol} of the low- z (T10; G13, red squares and blue triangles respectively) and high- z samples already presented in C21, including also our SUBWAYS measurements. For all samples, bolometric luminosities are consistently computed from the 2-10 keV luminosities assuming a luminosity-dependent bolometric correction (Duras et al. 2020). The best fit parameters of a linear relation in log space of $\log(v_{out}) = A(L_{bol})^B$ are $A = -3.88 \pm 1.40$ and $B = 0.19 \pm 0.03$. Overall, the SUBWAYS data fit right between the low- and the high- z data. We find a Kendall's (rank) correlation coefficient of $\tau = 0.45$ with a null probability of $p_{null} = 1.8 \times 10^{-7}$. The strength and slope of this correlation is partially driven by the 6 data-points in C21, with $\log(L_{bol}/\text{erg s}^{-1}) \geq 48$, that may be affected by additional uncertainties associated with the magnification factor due to lensing.

The low- and high- z fit correlation in C21 (see their Table 10) returned a slope of $B = 0.20 \pm 0.03$, a correlation coefficient of $\tau = 0.51$ with a null probability $p_{null} = 6.0 \times 10^{-8}$. Their slope

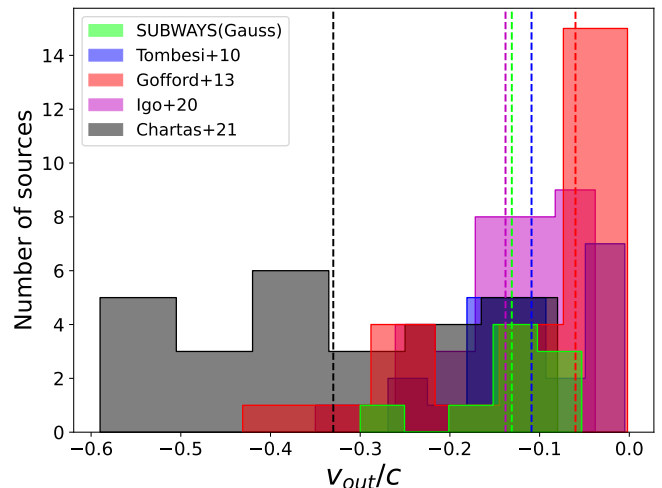


Fig. 7: Distributions and mean outflow velocity values, indicated by the vertical dashed lines, as measured in this work (SUBWAYS) $\bar{v}_{out} = -0.133c$; T10 $\bar{v}_{out} = -0.109c$; G13 $\bar{v}_{out} = -0.056c$; Igo20 $\bar{v}_{out} = -0.138c$, C21 $\bar{v}_{out} = -0.330c$.

is consistent with our measurement, whereas their coefficient is about 10% higher, which is suggesting that our correlation, with all the 4 samples included, is slightly weaker than in C21. A similar correlation was also observed by Matzeu et al. (2017) in the luminous QSO PDS 456 between the *XMM-Newton*, *NuSTAR* and *Suzaku* observation from 2001–2014. The slope of the correlation in Matzeu et al. (2017, i.e., 0.22 ± 0.04) is largely consistent with what we have found here.

Overall, with our result we can conclude that there is a correlation between the outflow velocities and bolometric luminosities within the overall low- intermediate- high- z samples. A positive correlation with a slope of 0.5 between outflow velocities and the luminosities of the AGN is what it would be expected in a radiatively-driven wind scenario as the radiation pressure plays a key role in driving the outflows.

The fact that the observed slope is lower than the expected value can be explained in several ways. One possible explanation, already suggested in C21, is that we did not include outflows with velocities $\lesssim 10000 \text{ km s}^{-1}$, as in T10.

Another plausible explanation is that, as the luminosity keep increasing, the inner part of the UFOs detected in SUBWAYS might be over-ionised, with weaker absorption features (e.g., Parker et al. 2017; Pinto et al. 2018) leading to their observability being pushed to the outer streamlines. Within this regime the observed velocities, due to their radial dependence, would appear slightly slower and such a physical condition leads to an overall flattening of the slope (Matzeu et al. 2017) from the nominal value of 0.5. The outflows shown in Figure 8 have a range of mass outflow rates and black hole masses, so it is not clear that a simple scaling of velocity with luminosity is likely. If instead we assume that all the systems are close to their Eddington luminosities L_{Edd} and the outflows have the Eddington momenta L_{Edd}/c (see e.g. King 2003; King & Pounds 2015, and references therein) one finds that the velocities should be of order $0.1c$, as observed (see also Figure 7).

In reality, the driving (and launching) mechanism responsible for the observed UFOs are likely the result of a complex interaction between radiation pressure and MHD driving. Indeed, it

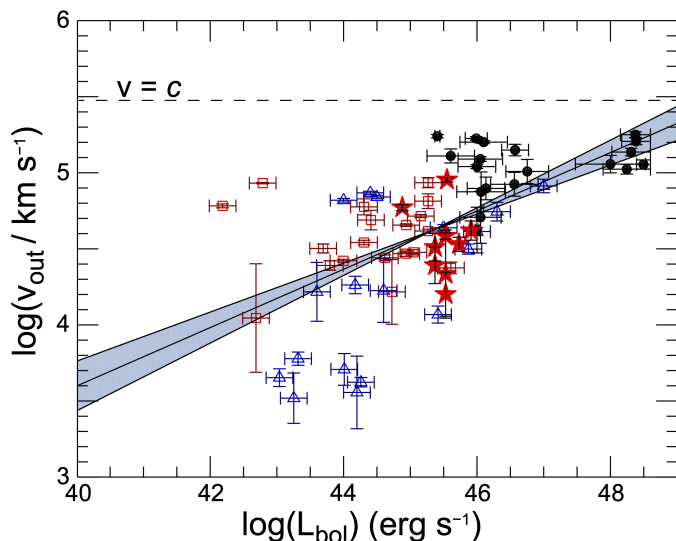


Fig. 8: Outflow velocity of the ionised absorber for our SUBWAYS targets (red filled stars) plotted against their bolometric luminosity. Also plotted are the same quantities as derived in the analysis of the low- z AGN samples of Tombesi et al. (2012, red empty squares), G13, (blue empty triangles) and in the high- z AGN sample of C21, (black filled circles). The power-law least-squares fit to the combined samples (a total of 49 individual objects and 63 observations) is shown with a solid line. The shaded area represents the uncertainty of the slopes of our fits to the data. Here the outflow velocity is simply described as the absolute value of v_{out} .

was previously found, in Matzeu et al. (2016) that in the powerful disk-wind observed in PDS 456 in 2013, the radiation pressure alone, imparted from a strong flare, could have not deposit enough kinetic power on the outflowing material and hence suggesting that an additional launching mechanism, such as MHD, was also involved. Decoupling and assessment of each individual contribution remains a challenging subject in disk-wind physics with the current CCD detectors.

6.2. Strong features around rest-energies of 9 keV

In our SUBWAYS sample, the Fe K absorption line with the highest degree of blueshift was detected in PG 0947+396 (Obs1) at $E_{\text{rest}} = 9.5 \pm 0.1$ keV ($E_{\text{obs}} \sim 7.9$ keV).

Despite its reasonable significance (see Table 2), there are a few caveats that could rule out its UFO identification. The energy shift from the H-like iron rest-energy is rather large (even larger if He-like Fe is considered), and corresponds to an outflow velocity of $v_{\text{out}} = -0.30 \pm 0.01c$, which is, by far, the fastest of the sample. Such result could be (in principle) at odds considering the relatively low-Eddington fraction of this source i.e., $L_{\text{bol}}/L_{\text{Edd}} \sim 0.06$. These kind of outflow velocities are more common in sources that are accreting near or above their Eddington limit, e.g. PDS 456. In this campaign, a second ~ 60 ks observation (PG 0947+396 Obs2) was carried out about 5 months later and no Fe K absorption line was detected in the spectra (see Figure E.1). The same applies for the first 20 ks *XMM-Newton* observation in 2001. Having said that, it is not impossible to have such powerful UFO in a low-Eddington regime as other driving mechanisms, such as MHD, could play a key role (e.g., Fuku-

mura et al. 2017). Indeed, further monitoring of this source will shed some light on the presence of an UFO.

Strong residuals in emission at $E_{\text{rest}} \sim 9$ keV are detected in 2MASS J165315+2349 and PG1114+445 (0651330801) at the $P_{\text{F}} > 99\%$ confidence level, which might be associated with a possible high-order iron K transition or perhaps associated with an instrumental calibration artifact. The origin of this feature could be associated with $\text{Ni xxvii He}\beta 1s \rightarrow 3p$, or a blend thereof, however no lower transitions are observed in the spectra. Such a feature is also observed in PG 1114+445, as blueshifted $\text{Fe xxvi Ly}\beta$ (8.25 keV). The dominant emission line in the pn background is the $\text{Cu K}\alpha$ line at 8.04 keV. Weaker surrounding lines include $\text{Ni K}\alpha$ (7.47 keV), $\text{Zn K}\alpha$ (8.63 keV) and $\text{Cu K}\beta$ (8.90 keV).

So another possible origin of these spurious features might arise from background subtraction issues during the data reduction process, or even from the detector itself such as in PG 1114+445. After a careful check we confirm that the line detections are genuine as no such issues were found. A thorough characterization of the physical properties of the winds responsible for the detected Fe K lines will be carried out by using physically motivated models such as *XSTAR*, *XABS*, *WINE* (Luminari et al. 2021) and *XRADE* (Matzeu et al. 2022), and will be presented in a forthcoming SUBWAYS paper.

A second absorption line at $E_{\text{rest}} \sim 11$ keV ($E_{\text{obs}} \sim 9$ keV) is detected in LBQS 1338–0038 at the $P_{\text{F}} = 99.3\%$ confidence level however, following a *MC* procedure the significance of the line drops considerably to $P_{\text{MC}} = 87.2\%$. This discrepancy in the detection can be likely attributed to the lack of data at energies $E_{\text{obs}} > 10$ keV being at the edge of the *XMM-Newton* bandpass, and hence extra care is needed. Nonetheless, this high energy absorption feature is also present during a ~ 50 ks *NuSTAR* exposure one year later in 2020 (PI Bianchi). A joint analysis focused on of the *XMM-Newton* and *NuSTAR* data of LBQS 1338–0038 will be presented in a companion letter (Matzeu et al., in prep.).

7. Summary and Conclusions

We carried out a systematic search focused on absorption features in the Fe K band in a sample of 22 (41 observations) luminous ($2 \times 10^{45} \lesssim L_{\text{bol}}/\text{erg s}^{-1} \lesssim 2 \times 10^{46}$) active galactic nuclei (AGN) at intermediate redshift ($0.1 \lesssim z \lesssim 0.4$), as part of the large *XMM-Newton* program SUBWAYS. For each *XMM-Newton* observation, the data reduction was performed by optimising the level of background in order to increase of the signal-to-noise (SNR) between the 4–10 keV band. Afterwards, an additional and crucial step was the appropriate choice of an optimal spectral binning in order to avoid loss of information for any search of weak features like UFOs. We applied the four spectral binning that are most used in the literature and subsequently after cross-checking them all our results are based on the \mathcal{KB} binning.

The main results are summarised below:

- We carried out an *XMM-Newton* broadband analysis between 0.3–10 keV. We find that in 27 out of 41 observations ($\sim 65\%$) our targets have intrinsic absorption in the soft X-rays, of which ($\sim 70\%$) can be identified as fully covering, mildly ionised (warm) absorbers and 5/27 ($\sim 30\%$) are partially covering the line-of-sight.
- We then analysed the EPIC spectra of each of the 41 observations by first performing a series of blind-search line scans, in both emission and absorption, focused on the 5–10 keV band. For the overall Fe K emissions, the energies range

between $6.2 \lesssim E_{\text{rest}}/\text{keV} \lesssim 9$ where $\sim 90\%$ are consistent with the Fe K α core (detected in 20/22 targets) and $\sim 36\%$ consistent with Fe xxv–xxvi (detected in 8/22 targets). Their equivalent width ranges between $10 \lesssim EW/\text{eV} \lesssim 468$, where the high-end values are due to complex emission features such as in PG 1352+183, likely arising from a blend between Fe K $\alpha[\beta]$ and Fe xxv.

- For the Fe K absorption features we detected 14 absorption lines at the $P_F \gtrsim 99\%$ confidence level with energies ranging between $7 \lesssim E_{\text{rest}}/\text{keV} \lesssim 11$, where $\sim 85\%$ are consistent with Fe xxv–xxvi and one detection is consistent with an iron K edge. Their equivalent widths are ranging between $-200 \lesssim EW/\text{eV} \lesssim -40$, which are in line with what is expected for relatively narrow Fe K absorption profiles.
- Thanks to extensive Monte Carlo simulations, we confirmed absorption lines corresponding to highly ionised iron in 7/22 sources. These findings yield an UFO detection fraction of $\sim 30\%$ on the total sample, at a $P_{MC} \gtrsim 95\%$ significance level. These features likely correspond to either Fe xxv He α and/or Fe xxvi Ly α . By using the Fe xxvi lab transition as reference energy, we measure outflow velocities ranging between $-0.3 \lesssim v_{\text{out}}/c \lesssim -0.05$ with average and median velocities of $\bar{v}_{\text{out}} = -0.133c$ and $\tilde{v}_{\text{out}} = -0.110c$.
- In this work we also presented preliminary results of photoionisation modelling of the iron K features detected at the $P_{MC} \gtrsim 95\%$ confidence level, with xSTAR. We find median values of $\log(\tilde{N}_{\text{H}}/\text{cm}^{-2}) \sim 23.8$ and $\log(\tilde{\xi}/\text{erg cm s}^{-1}) \sim 4.8$ for the column densities and ionization parameter, respectively.
- The measured outflow velocities with xSTAR are ranging between $-0.3 \lesssim v_{\text{out}}/c \lesssim -0.1$, where the mean/median values are $\bar{v}_{\text{out}} \sim -0.144$ and $\tilde{v}_{\text{out}} \sim -0.110$, respectively. Such distribution is largely comparable with the outflow velocities measured with the phenomenological (Gaussian) modelling. Such results confirm that the absorption detected in the Fe K band arise from fast highly ionised material with high column density as typically observed in UFOs.
- By comparing our results with previous work, we computed a power-law least-squares fit to the low- z (T10; G13), intermediate- z (SUBWAYS) and high- z (C21) data, which show a positive correlation between outflow velocity and bolometric luminosity within the overall low-intermediate-high z samples, with slope 0.19 ± 0.03 . Such $v_{\text{out}}-L_{\text{bol}}$ correlation is also observed in Matzeu et al. (2017) with a slope of 0.22 ± 0.04 .

The outcome of this work independently provides further support for the existence of highly ionised matter propagating at mildly relativistic speed, which are expected to play a key role in the self-regulated AGN feeding-feedback loop that shapes galaxies, as shown by hydrodynamical multi-phase simulations (Gaspari et al. 2020, for a review). These results suggest that the likely dominant driving mechanisms of UFOs is radiation pressure arising in high-accretion regimes. It is important to note that MHD also play a key role in the driving and launching mechanism of disk-winds and future observations at micro-calorimeter resolution will contribute towards distinguishing each component.

An alternative scenario that has been put forward is that the origin of Fe K absorption features can be attributed to a layer of hot gas located at the surface of the accretion disk rather than from an outflowing wind (Gallo et al. 2013). Thus the prominent and blueshifted absorption lines are the result of strong relativistic reflection component that dominate the hard X-ray continuum rather than the primary emission. Such model was successfully applied to NLSy1 IRAS13224–3809 by Fabian et al. (2020). The unprecedented spectral micro-calorimeter resolution from future UFOs observations, such as XRISM/Resolve (and Athena/X-IFU), will greatly contribute towards disentangling each of these scenarios including the disk-wind’s launching/driving physical mechanism (e.g., Giustini & Proga 2012; Fukumura et al. 2022; Dadina et al.: in preparation; Matzeu et al.: in preparation).

Acknowledgements. GAM and all the Italian co-authors acknowledge support and fundings from Accordo Attuativo ASI-INAF n. 2017-14-H.0. MB is supported by the European Union’s Horizon 2020 research and innovation programme Marie Skłodowska-Curie grant No 860744 (BID4BEST). MG acknowledges partial support by HST GO-15890.020/023-A, the *BlackHoleWeather* program, and NASA HEC Pleiades (SMD-1726). BDM acknowledges support via Ramón y Cajal Fellowship RYC2018-025950-I. SM is grateful for the NASA ADAP grant 80NSSC20K0438. AL acknowledges support from the HORIZON-2020 grant “Integrated Activities for the High Energy Astrophysics Domain” (AHEAD-2020), G.A. 871158. SRON is supported financially by NWO, the Netherlands Organization for Scientific Research. M.Gi. is supported by the “Programa de Atracción de Talento” of the Comunidad de Madrid, grant number 2018-T1/TIC-11733. We warmly thank Katia Gkimisi and Raffaella Morganti for useful discussions.

References

- Aird, J., Coil, A. L., Georgakakis, A., et al. 2015, *MNRAS*, 451, 1892
- Arnaud, K. A. 1996, in *Astronomical Society of the Pacific Conference Series*, Vol. 101, *Astronomical Data Analysis Software and Systems V*, ed. G. H. Jacoby & J. Barnes, 17
- Ballantyne, D. R. & Xiang, X. 2020, *MNRAS*, 496, 4255
- Bautista, M. A. & Kallman, T. R. 2001, *ApJS*, 134, 139
- Bertola, E., Dadina, M., Cappi, M., et al. 2020, *A&A*, 638, A136
- Bianchi, S., Guainazzi, M., Matt, G., Fonseca Bonilla, N., & Ponti, G. 2009, *A&A*, 495, 421
- Bischetti, M., Maiolino, R., Carniani, S., et al. 2019a, *A&A*, 630, A59
- Bischetti, M., Piconcelli, E., Feruglio, C., et al. 2019b, *A&A*, 628, A118
- Blustin, A. J., Page, M. J., Fuerst, S. V., Branduardi-Raymont, G., & Ashton, C. E. 2005, *A&A*, 431, 111
- Boller, T., Liu, T., Weber, P., et al. 2021, *A&A*, 647, A6
- Braitto, V., Reeves, J. N., Gofford, J., et al. 2014, *ApJ*, 795, 87
- Braitto, V., Reeves, J. N., Matzeu, G. A., et al. 2018, *MNRAS*, 479, 3592
- Brusa, M., Bongiorno, A., Cresci, G., et al. 2015, *MNRAS*, 446, 2394
- Brusa, M., Cresci, G., Daddi, E., et al. 2018, *A&A*, 612, A29
- Cash, W. 1979, *ApJ*, 228, 939
- Chartas, G., Brandt, W. N., Gallagher, S. C., & Garmire, G. P. 2002, *ApJ*, 579, 169
- Chartas, G. & Canas, M. H. 2018, *ApJ*, 867, 103
- Chartas, G., Cappi, M., Vignali, C., et al. 2021, *ApJ*, 920, 24
- Chartas, G., Charlton, J., Eracleous, M., et al. 2009, *New A Rev.*, 53, 128
- Cicone, C., Maiolino, R., Sturm, E., et al. 2014, *A&A*, 562, A21
- Cicone, C., Severgnini, P., Papadopoulos, P. P., et al. 2018, *ApJ*, 863, 143
- Costa, T., Sijacki, D., & Haehnelt, M. G. 2014, *MNRAS*, 444, 2355
- Crenshaw, D. M., Kraemer, S. B., & George, I. M. 2003, *ARA&A*, 41, 117
- Cresci, G., Mainieri, V., Brusa, M., et al. 2015, *ApJ*, 799, 82
- Dadina, M., Vignali, C., Cappi, M., et al. 2016, *A&A*, 592, A104
- Dadina et al.: in preparation
- Dauser, T., García, J., Parker, M. L., Fabian, A. C., & Wilms, J. 2014, *MNRAS*, 444, L100
- Di Matteo, T., Springel, V., & Hernquist, L. 2005, *Nature*, 433, 604
- Done, C., Davis, S. W., Jin, C., Blaes, O., & Ward, M. 2012, *MNRAS*, 420, 1848
- Duras, F., Bongiorno, A., Ricci, F., et al. 2020, *A&A*, 636, A73
- Eckert, D., Gaspari, M., Gastaldello, F., Le Brun, A. M. C., & O’Sullivan, E. 2021, *Universe*, 7, 142
- Fabian, A. C. 2012, *ARA&A*, 50, 455
- Fabian, A. C., Reynolds, C. S., Jiang, J., et al. 2020, *MNRAS*, 493, 2518
- Feruglio, C., Ferrara, A., Bischetti, M., et al. 2017, *A&A*, 608, A30
- Feruglio, C., Fiore, F., Carniani, S., et al. 2015, *A&A*, 583, A99
- Feruglio, C., Maiolino, R., Piconcelli, E., et al. 2010, *A&A*, 518, L155

- Fiore, F., Feruglio, C., Shankar, F., et al. 2017, *A&A*, 601, A143
- Fukumura, K., Dadina, M., Matzeu, G., et al. 2022, *ApJ*, 940, 6
- Fukumura, K., Kazanas, D., Contopoulos, I., & Behar, E. 2010, *ApJ*, 715, 636
- Fukumura, K., Kazanas, D., Shrader, C., et al. 2017, *Nature Astronomy*, 1, 0062
- Gabriel, C., Denby, M., Fyfe, D. J., et al. 2004, *Astronomical Society of the Pacific Conference Series*, Vol. 314, *The XMM-Newton SAS - Distributed Development and Maintenance of a Large Science Analysis System: A Critical Analysis*, ed. F. Ochsenbein, M. G. Allen, & D. Egret, 759
- Gallo, L. C., Fabian, A. C., Grupe, D., et al. 2013, *MNRAS*, 428, 1191
- García, J., Dauser, T., Lohfink, A., et al. 2014, *ApJ*, 782, 76
- García, J., Dauser, T., Reynolds, C. S., et al. 2013, *ApJ*, 768, 146
- García, J. A., Kara, E., Walton, D., et al. 2019, *ApJ*, 871, 88
- Gaskell, C. M. 1982, *ApJ*, 263, 79
- Gaspari, M., Brighenti, F., & Ruszkowski, M. 2013, *Astronomische Nachrichten*, 334, 394
- Gaspari, M., Eckert, D., Etori, S., et al. 2019, *ApJ*, 884, 169
- Gaspari, M. & Sądowski, A. 2017, *ApJ*, 837, 149
- Gaspari, M., Temi, P., & Brighenti, F. 2017, *MNRAS*, 466, 677
- Gaspari, M., Tombesi, F., & Cappi, M. 2020, *Nature Astronomy*, 4, 10
- Giustini, M. & Proga, D. 2012, *ApJ*, 758, 70
- Giustini, M. & Proga, D. 2019, *A&A*, 630, A94
- Gofford, J., Reeves, J. N., McLaughlin, D. E., et al. 2015, *MNRAS*, 451, 4169
- Gofford, J., Reeves, J. N., Tombesi, F., et al. 2013, *MNRAS*, 430, 60
- Green, J. C., Froning, C. S., Osterman, S., et al. 2012, *ApJ*, 744, 60
- Halpern, J. P. 1984, *ApJ*, 281, 90
- Hamann, F., Chartas, G., Reeves, J., & Nardini, E. 2018, *MNRAS*, 476, 943
- Harrison, C. M., Alexander, D. M., Mullaney, J. R., & Swinbank, A. M. 2014, *MNRAS*, 441, 3306
- Heckman, T. M. & Best, P. N. 2014, *ARA&A*, 52, 589
- HI4PI Collaboration, Ben Bekhti, N., Flöer, L., et al. 2016, *A&A*, 594, A116
- Hurkett, C. P., Vaughan, S., Osborne, J. P., et al. 2008, *ApJ*, 679, 587
- Igo, Z., Parker, M. L., Matzeu, G. A., et al. 2020, *MNRAS*, 493, 1088
- Jansen, F., Lumb, D., Altieri, B., et al. 2001, *A&A*, 365, L1
- Jiang, J., Fabian, A. C., Dauser, T., et al. 2019, *MNRAS*, 489, 3436
- Kaastra, J. S. & Bleeker, J. A. M. 2016, *A&A*, 587, A151
- Kaastra, J. S., Kriss, G. A., Cappi, M., et al. 2014, *Science*, 345, 64
- Kaastra, J. S., Mewe, R., Liedahl, D. A., Komossa, S., & Brinkman, A. C. 2000, *A&A*, 354, L83
- Kaastra, J. S., Mewe, R., & Nieuwenhuijzen, H. 1996, in *UV and X-ray Spectroscopy of Astrophysical and Laboratory Plasmas*, 411–414
- Kallman, T. R., Palmeri, P., Bautista, M. A., Mendoza, C., & Krolik, J. H. 2004, *ApJS*, 155, 675
- Kaspi, S., Brandt, W. N., Netzer, H., et al. 2000a, *ApJ*, 535, L17
- Kaspi, S., Smith, P. S., Netzer, H., et al. 2000b, *ApJ*, 533, 631
- King, A. 2003, *ApJ*, 596, L27
- King, A. 2005, *ApJ*, 635, L121
- King, A. & Pounds, K. 2015, *ARA&A*, 53, 115
- King, A. R., Zubovas, K., & Power, C. 2011, *MNRAS*, 415, L6
- Kormendy, J. & Ho, L. C. 2013, *ARA&A*, 51, 511
- Kraemer, S. B., Tombesi, F., & Bottorff, M. C. 2018, *ApJ*, 852, 35
- Kriss, G. A., Lee, J. C., Danekhar, A., et al. 2018, *ApJ*, 853, 166
- Kriss, G. A., Mehdipour, M., Kaastra, J. S., et al. 2019, *A&A*, 621, A12
- Krongold, Y., Longinotti, A. L., Santos-Lleo, M., et al. 2021, *ApJ*, 917, 39
- Laha, S., Guainazzi, M., Chakravorty, S., Dewangan, G. C., & Kembhavi, A. K. 2016, *MNRAS*, 457, 3896
- Laha, S., Guainazzi, M., Dewangan, G. C., Chakravorty, S., & Kembhavi, A. K. 2014, *MNRAS*, 441, 2613
- Laha, S., Reynolds, C. S., Reeves, J., et al. 2021, *Nature Astronomy*, 5, 13
- Lanzuisi, G., Giustini, M., Cappi, M., et al. 2012, *A&A*, 544, A2
- Longinotti, A. L., Krongold, Y., Guainazzi, M., et al. 2015, *ApJ*, 813, L39
- Longinotti, A. L., Vega, O., Krongold, Y., et al. 2018, *ApJ*, 867, L11
- Luminari, A., Nicastro, F., Elvis, M., et al. 2021, *A&A*, 646, A111
- Luminari, A., Piconcelli, E., Tombesi, F., et al. 2018, *A&A*, 619, A149
- Maccagni, F. M., Serra, P., Gaspari, M., et al. 2021, *A&A*, 656, A45
- Magorrian, J., Tremaine, S., Richstone, D., et al. 1998, *AJ*, 115, 2285
- Maiolino, R., Gallerani, S., Neri, R., et al. 2012, *MNRAS*, 425, L66
- Mallick, L., Fabian, A. C., García, J. A., et al. 2022, *MNRAS*, 513, 4361
- Marasco, A., Cresci, G., Nardini, E., et al. 2020, *A&A*, 644, A15
- Markowitz, A., Reeves, J. N., & Braitto, V. 2006, *ApJ*, 646, 783
- Mathur, S., Wilkes, B., & Elvis, M. 1998, *ApJ*, 503, L23
- Mathur, S., Wilkes, B. J., & Aldcroft, T. 1997, *ApJ*, 478, 182
- Matzeu, G. A., Lieu, M., Costa, M. T., et al. 2022, *MNRAS*, 515, 6172
- Matzeu, G. A., Reeves, J. N., Braitto, V., et al. 2017, *MNRAS*, 472, L15
- Matzeu, G. A., Reeves, J. N., Nardini, E., et al. 2016, *MNRAS*, 458, 1311
- Matzeu et al.: in preparation
- McKernan, B., Yaqoob, T., & Reynolds, C. S. 2007, *MNRAS*, 379, 1359
- McKinley, B., Tingay, S. J., Gaspari, M., et al. 2022, *Nature Astronomy*, 6, 109
- Mehdipour, M., Kriss, G. A., Krongold, Y., et al. 2022, *arXiv e-prints*, arXiv:2202.08405
- mehdipour et al. 2022.: in press
- Middei, R., Bianchi, S., Cappi, M., et al. 2018, *A&A*, 615, A163
- Middei, R., Tombesi, F., Vagnetti, F., et al. 2020, *A&A*, 635, A18
- Miniutti, G. & Fabian, A. C. 2006, *MNRAS*, 366, 115
- Mizumoto, M., Done, C., Tomaru, R., & Edwards, I. 2019, *MNRAS*, 489, 1152
- Morganti, R., Tadhunter, C. N., & Oosterloo, T. A. 2005, *A&A*, 444, L9
- Murphy, E. M., Lockman, F. J., Laor, A., & Elvis, M. 1996, *ApJS*, 105, 369
- Murray, N., Chiang, J., Grossman, S. A., & Voit, G. M. 1995, *ApJ*, 451, 498
- Murray, N., Quataert, E., & Thompson, T. A. 2005, *ApJ*, 618, 569
- Nardini, E., Fabian, A. C., Reis, R. C., & Walton, D. J. 2011, *MNRAS*, 410, 1251
- Nardini, E., Lusso, E., & Bisogni, S. 2019, *MNRAS*, 482, L134
- Nardini, E., Reeves, J. N., Gofford, J., et al. 2015, *Science*, 347, 860
- Nardini, E. & Zubovas, K. 2018, *MNRAS*, 478, 2274
- Ostriker, J. P., Choi, E., Ciotti, L., Novak, G. S., & Proga, D. 2010, *ApJ*, 722, 642
- Parker, M. L., Alston, W. N., Igo, Z., & Fabian, A. C. 2020, *MNRAS*, 492, 1363
- Parker, M. L., Longinotti, A. L., Schartel, N., et al. 2019a, *MNRAS*, 490, 683
- Parker, M. L., Longinotti, A. L., Schartel, N., et al. 2019b, *MNRAS*, 490, 683
- Parker, M. L., Matzeu, G. A., Guainazzi, M., et al. 2018, *MNRAS*, 480, 2365
- Parker, M. L., Pinto, C., Fabian, A. C., et al. 2017, *Nature*, 543, 83
- Perna, M., Lanzuisi, G., Brusa, M., Mignoli, M., & Cresci, G. 2017, *A&A*, 603, A99
- Petrucci, P. O., Paltani, S., Malzac, J., et al. 2013, *A&A*, 549, A73
- Petrucci, P.-O., Ursini, F., De Rosa, A., et al. 2018, *A&A*, 611, A59
- Piconcelli, E., Jimenez-Bailón, E., Guainazzi, M., et al. 2004, *MNRAS*, 351, 161
- Piconcelli, E., Jimenez-Bailón, E., Guainazzi, M., et al. 2005, *A&A*, 432, 15
- Pinto, C., Alston, W., Parker, M. L., et al. 2018, *MNRAS*, 476, 1021
- Porquet, D., Kaastra, J. S., Page, K. L., et al. 2004a, *A&A*, 413, 913
- Porquet, D., Reeves, J. N., Grosso, N., Braitto, V., & Lobban, A. 2021, *A&A*, 654, A89
- Porquet, D., Reeves, J. N., Uttley, P., & Turner, T. J. 2004b, *A&A*, 427, 101
- Pounds, K. A. & Reeves, J. N. 2009, *MNRAS*, 397, 249
- Proga, D., Stone, J. M., & Kallman, T. R. 2000, *ApJ*, 543, 686
- Protosov, R., van Dyk, D. A., Connors, A., Kashyap, V. L., & Siemiginowska, A. 2002, *ApJ*, 571, 545
- Reeves, J. N. & Braitto, V. 2019, *ApJ*, 884, 80
- Reeves, J. N., Braitto, V., Chartas, G., et al. 2020, *ApJ*, 895, 37
- Reeves, J. N., Braitto, V., Nardini, E., et al. 2016, *ApJ*, 824, 20
- Reeves, J. N., Braitto, V., Nardini, E., et al. 2018a, *ApJ*, 854, L8
- Reeves, J. N., Lobban, A., & Pounds, K. A. 2018b, *ApJ*, 854, 28
- Reeves, J. N., O'Brien, P. T., & Ward, M. J. 2003, *ApJ*, 593, L65
- Reeves, J. N., Porquet, D., Braitto, V., et al. 2013, *ApJ*, 776, 99
- Reynolds, C. S. 1997, *MNRAS*, 286, 513
- Richards, G. T., Kruczek, N. E., Gallagher, S. C., et al. 2011, *AJ*, 141, 167
- Ross, R. F. & Fabian, A. C. 2005, *MNRAS*, 358, 211
- Różańska, A., Malzac, J., Belmont, R., Czerny, B., & Petrucci, P. O. 2015, *A&A*, 580, A77
- Saez, C. & Chartas, G. 2011, *ApJ*, 737, 91
- Sako, M., Kahn, S. M., Paerels, F., & Liedahl, D. A. 2000, *ApJ*, 543, L115
- Salpeter, E. E. 1964, *ApJ*, 140, 796
- Schmidt, M. & Green, R. F. 1983, *ApJ*, 269, 352
- Serafinelli, R., Tombesi, F., Vagnetti, F., et al. 2019, *A&A*, 627, A121
- Sim, S. A., Long, K. S., Miller, L., & Turner, T. J. 2008, *MNRAS*, 388, 611
- Sim, S. A., Miller, L., Long, K. S., Turner, T. J., & Reeves, J. N. 2010, *MNRAS*, 404, 1369
- Sirressi, M., Ciccone, C., Severgnini, P., et al. 2019, *MNRAS*, 489, 1927
- Sądowski, A. & Gaspari, M. 2017, *MNRAS*, 468, 1398
- Smith, R. K., Brickhouse, N. S., Liedahl, D. A., & Raymond, J. C. 2001, *ApJ*, 556, L91
- Steenbrugge, K. C., Kaastra, J. S., Crenshaw, D. M., et al. 2005, *A&A*, 434, 569
- Steenbrugge, K. C., Kaastra, J. S., de Vries, C. P., & Edelson, R. 2003, *A&A*, 402, 477
- Strüder, L., Briel, U., Dennerl, K., et al. 2001, *A&A*, 365, L18
- Temi, P., Gaspari, M., Brighenti, F., et al. 2022, *ApJ*, 928, 150
- Tombesi, F., Cappi, M., Reeves, J. N., & Braitto, V. 2012, *MNRAS*, 422, L1
- Tombesi, F., Cappi, M., Reeves, J. N., et al. 2013, *MNRAS*, 430, 1102
- Tombesi, F., Cappi, M., Reeves, J. N., et al. 2011, *ApJ*, 742, 44
- Tombesi, F., Cappi, M., Reeves, J. N., et al. 2010, *A&A*, 521, A57
- Tombesi, F., Meléndez, M., Veilleux, S., et al. 2015, *Nature*, 519, 436
- Torrey, P., Hopkins, P. F., Faucher-Giguère, C.-A., et al. 2020, *MNRAS*, 497, 5292
- Tozzi, G., Cresci, G., Marasco, A., et al. 2021, *A&A*, 648, A99
- Turner, M. J. L., Abbey, A., Arnaud, M., et al. 2001, *A&A*, 365, L27
- Ursini, F., Petrucci, P. O., Bianchi, S., et al. 2020, *A&A*, 634, A92
- Vaughan, S., Edelson, R., Warwick, R. S., & Uttley, P. 2003, *MNRAS*, 345, 1271
- Vietri, G., Misawa, T., Piconcelli, E., et al. 2022, *arXiv e-prints*, arXiv:2205.06832
- Vignali, C., Iwasawa, K., Comastri, A., et al. 2015, *A&A*, 583, A141
- Walton, D. J., Nardini, E., Fabian, A. C., Gallo, L. C., & Reis, R. C. 2013, *MNRAS*, 428, 2901
- Waters, T., Proga, D., & Dannen, R. 2021, *ApJ*, 914, 62
- Wilkes, B. J. & Elvis, M. 1987, *ApJ*, 323, 243

Wilkins, D. R. & Fabian, A. C. 2012, MNRAS, 424, 1284
 Wilms, J., Allen, A., & McCray, R. 2000, ApJ, 542, 914
 Wittor, D. & Gaspari, M. 2020, MNRAS, 498, 4983
 Woods, D. T., Klein, R. I., Castor, J. I., McKee, C. F., & Bell, J. B. 1996, ApJ, 461, 767
 Xie, Y., Li, A., & Hao, L. 2017, ApJS, 228, 6
 Xu, Y., García, J. A., Walton, D. J., et al. 2021, ApJ, 913, 13
 Yang, H. Y. K., Gaspari, M., & Marlow, C. 2019, ApJ, 871, 6
 Zanchettin, M. V., Feruglio, C., Bischetti, M., et al. 2021, A&A, 655, A25
 Zubovas, K. & King, A. 2012, ApJ, 745, L34
 Zubovas, K. & King, A. 2016, MNRAS, 462, 4055
 Zubovas, K. & Nardini, E. 2020, MNRAS, 498, 3633

Road, Cambridge, CB3 0HA, UK; Cavendish Laboratory, University of Cambridge, 19 J. J. Thomson Avenue, Cambridge, CB3 0HE, UK
³²Max-Planck-Institut für extraterrestrische Physik, Giessenbachstraße 1, D-85748 Garching bei München, Germany

¹Department of Physics and Astronomy (DIFA), University of Bologna, Via Gobetti, 93/2, I-40129 Bologna, Italy

²INAF-Osservatorio di Astrofisica e Scienza dello Spazio di Bologna, Via Gobetti, 93/3, I-40129 Bologna, Italy

³European Space Agency (ESA), European Space Astronomy Centre (ESAC), E-28691 Villanueva de la Cañada, Madrid, Spain

⁴Dipartimento di Matematica e Fisica, Università degli Studi Roma Tre, Via della Vasca Navale 84, I-00146, Roma, Italy

⁵Space Telescope Science Institute, 3700 San Martin Drive, Baltimore, MD 21218, USA

⁶INAF – Osservatorio Astrofisico di Arcetri, Largo Enrico Fermi 5, I-50125 Firenze, Italy

⁷ Department of Physics and Astronomy, College of Charleston, Charleston, SC, 29424, USA

⁸Space Science Data Center - ASI, Via del Politecnico s.n.c., 00133 Roma, Italy

⁹INAF - Osservatorio Astronomico di Roma, Via Frascati 33, 00078, Monte Porzio Catone (Roma), Italy

¹⁰Univ. Grenoble Alpes, CNRS, IPAG, 38000, Grenoble, France

¹¹Instituto de Astronomía, Universidad Nacional Autónoma de México, Circuito Exterior, Ciudad Universitaria, Ciudad de México 04510, México

¹² Department of Physics, University of Rome ‘Tor Vergata’, Via della Ricerca Scientifica 1, I-00133 Rome, Italy

¹³ Department of Astronomy, University of Maryland, College Park, MD 20742, USA

¹⁴ NASA/Goddard Space Flight Center, Code 662, Greenbelt, MD 20771, USA

¹⁵ INAF — Istituto di Astrofisica e Planetologia Spaziali, Via Fosso del Cavaliere, I-00133 Roma, Italy

¹⁶Centro de Astrobiología (CSIC-INTA), Camino Bajo del Castillo s/n, Villanueva de la Cañada, E-28692 Madrid, Spain

¹⁷ Department of Astrophysical Sciences, Princeton University, 4 Ivy Lane, Princeton, NJ 08544-1001, USA

¹⁸Physics Department, The Technion, 32000, Haifa, Israel

¹⁹INAF - Osservatorio Astronomico di Trieste, Via G. B. Tiepolo 11, 34143, Trieste, Italy ²⁰Department of Astronomy, The Ohio State University, 140 West 18th Avenue, Columbus, OH 43210, USA

²¹Center for Cosmology and Astroparticle Physics, 191 West Woodruff Avenue, Columbus, OH 43210, USA ²²SRON Netherlands Institute for Space Research, Niels Bohrweg 4, 2333 CA Leiden, The Netherlands

²³ Departament de Física, EEBE, Universitat Politècnica de Catalunya, Av. Eduard Maristany 16, 08019 Barcelona, Spain

²⁴ESA - European Space Research and Technology Centre (ESTEC), Keplerlaan 1, 2201 AZ, Noordwijk, The Netherlands ²⁵Leiden Observatory, P.O. Box 9513, 2300 RA Leiden, The Netherlands

²⁶Department of Physics, Institute for Astrophysics and Computational Sciences, The Catholic University of America, Washington, DC, 20064, USA

²⁷ Dipartimento di Fisica e Astronomia, Università di Firenze, via G. Sansone 1, 50019 Sesto Fiorentino, Firenze, Italy

²⁸ INAF – Osservatorio Astronomico di Brera, Via Bianchi 46, I-23807 Merate (LC), Italy

²⁹Department of Physics & Astronomy, University of Nevada, Las Vegas, USA

³⁰ Department of Physics & Astronomy, University of Leicester, Leicester LE1 7RH, UK

³¹Kavli Institute for Cosmology, University of Cambridge, Madingley

Appendix A: Signal to noise optimization method

By following the [Piconcelli et al. \(2004\)](#) optimization method, we maximised the level of background that can be tolerated resulting into an increase of the SNR. This is carried out by testing, through an iterative process, different extraction source radii and for each radius the level of the background, defined as Max Background, is derived together with the corresponding SNR.

For observations that are not affected by background flares, the background level remains stable along the exposure and, consequently, we have no necessity to filter-out any particular time intervals. In this case the Max Background level is stable independently from the extraction region radius and the highest SNR is achieved at the maximum allowed extraction radius, that, in our case is $r = 40$ arcsec. Differently, for observations affected by strong background flares, the dimension of the extraction regions regulates the dominance of the source signal over the background and thus, the Max Background level changes as a function of the extraction radius itself. For those cases, the SNR depends on the interplay between the relative source dominance that tends to diminish as the source extraction radius increases leading to lower acceptable Max Background, and the overall source counts that tend to increase as the extraction radius increases. This interplay, at the end, defines a couple of values for the extraction radius and the Max Background for which we have the maximum SNR for our data. Between the extreme cases, we have observations for which there are short and/or weak background flares. In these cases we can appreciate some changes of the Max Background, but the best extraction region has the dimensions of maximum allowed radius. It is finally worth noting how the different effective areas among MOS and pn drive different instrument responses to background flares and, thus, different SNR and Max Background curves.

Appendix B: Summary of SUBWAYS observations

In [Table B.1](#) we summarise the individual observation details from the 22 SUBWAYS targets such as their ID, net exposure time and the corresponding total number of counts for each EPIC detector. We also tabulated the maximum signal-to-noise ratio obtained from our optimization procedure. We discarded all the observations with a total count $\lesssim 1500$ in the EPIC-pn.

Appendix C: Spectral binning

In this analysis we were interested in searching narrow and strong absorption features in the EPIC spectra. After maximizing the SNR, an additional and crucial step was to carefully include the appropriate choice of an optimal spectral binning in order to avoid the loss of information in the search of weak features like UFOs. We applied the four spectral binning methods most used in the literature (listed below) and subsequently cross-checked their results:

1. [*grpmin1*](#) - we over-sampled the EPIC-pn and EPIC-MOS resolution by imposing that each energy channel contains a minimum of 1 count through the `SPECGROUP` task within `SAS` (statistics: `Cstat`). This resulted in a binning resolution of $\Delta E = 5$ eV and 15 eV per energy bin throughout the 0.3–10 keV energy band for pn and MOS respectively for all the observations.
2. [*SN5*](#) - the data were binned to ensure a significance of at least 5σ per energy channel with `SPECGROUP` (statistics: χ^2). For the pn, such binning resulted in a binning resolution of

$\Delta E = 5$ eV at 1 keV and $\Delta E \sim 20$ eV at 6.4 keV, whilst $\Delta E = 15$ eV and $\Delta E \sim 60$ eV for MOS.

3. [*OS3grp20*](#) - this binning (also obtained with `SPECGROUP`) is commonly adopted in the literature and corresponds to an oversampling approximately $3\times$ of the instrumental FWHM. Additionally, the data are grouped to a minimum of 20 counts per bin in order to use χ^2 statistics. This binning prescription is a safe approach especially in cases where the level of significance of the measured signal is not known a priori. Such binning yielded a resolution of $\Delta E \sim 40$ eV, ~ 45 eV at 1 keV and $\Delta E \sim 75$ eV, 80 eV at 6.4 keV in EPIC-pn and -MOS respectively.
4. [Kaastra–Bleeker \(*KB*\)](#) - the [Kaastra & Bleeker \(2016\)](#) optimal binning option in `FTGROUPPHA` task within the `HEASOFT` package (statistics: `Cstat`) in order to maximise the signal in the spectra. In this sophisticated method, a variable binning scheme is followed so that each bin resolution matches the CCDs FWHM energy resolution of the EPIC detectors (or at least is not smaller than $1/3$). Depending on the spectra in question, the *KB* binning produced a EPIC-pn data resolution ranging between $\Delta E \sim 50$ –70 eV and $\Delta E \sim 100$ –150 eV at 1 keV and 6.4 keV and a EPIC-MOS resolution between $\Delta E \sim 40$ –60 eV and $\Delta E \sim 100$ –140 eV at 1 and 6.4 keV.

Appendix D: Broadband continuum modelling

In this work, despite being mainly focused on the iron K band, we carefully modelled the 0.3 – 10 keV continuum with the simplest phenomenological solution see [Equation 1](#). The summary of the best-fitting continuum parameters and the overall statistics, including for each EPIC detector, are tabulated in [Table D.1](#). In [Figure D.1](#) we show the individual plots for each SUBWAYS observation as per in [Figure 3](#). It is important to note that the final errors for the best-fit continuum models are recalculated and propagated to the final continuum plus iron K emission/absorption lines model.

Table B.1: (1) Source name; (2) Starting date of observation; (3) Net exposure after background optimization; (4) EPIC optimum SNR in the 4–10 keV (pn) and 0.3–10 keV (MOS) band and it is not reported in coadded spectra; (5) EPIC total net count in the 4–10 keV band.

Optimised EPIC Data Reduction:4–10 keV Band											
Source ¹	XMM ObsID	Date ² yyyy-mm-dd	Net Exposure ³ (ksec)			maxSNR ⁴			Total counts ⁵		
			pn	MOS 1	MOS 2	pn	MOS 1	MOS 2	pn	MOS 1	MOS 2
SUBWAYS targets observed during AO18 cycle											
PG0052+251	0841480101	2019-07-15	34.4	50.1	50.1	92.3	236.2	238.9	9119	3771	4229
PG0953+414	0841480201	2020-04-14	45.5	50.9	50.9	69.2	208.8	204.9	5244	1869	1897
PG1626+554	0841480401	2019-05-27	51.4	60.9	60.9	72.2	205.4	206.4	5902	2300	2375
PG1202+281	0841480501	2020-06-29	46.8	54.9	57.6	78.6	179.1	181.8	7141	2671	2746
PG1435–067	0841480601	2019-07-24	42.3	59.4	64.3	39.8	108.4	112.7	2022	899	973
SDSS J144414+0633	0841480701	2019-07-28	66.3	80.0	82.7	78.1	188.1	193.9	7067	2480	2774
2MASS J165315+2349	0841480801	2020-02-11	59.8	78.0	78.6	82.3	57.9	63.1	7652	2641	3039
PG1216+069	0841480901	2020-06-05	63.4	78.6	81.2	65.2	164.7	167.9	4792	1807	1902
PG0947+396	0841481001 (Obs 1)	2019-11-25	31.1	43.9	44.8	32.9	100.8	105.9	1682	789	847
	0841482301 (Obs 2)	2020-04-17	45.7	54.1	54.1	45.6	119.3	117.5	2436	908	947
WISE J053756–0245	0841481101	2020-03-02	69.8	90.3	91.4	57.6	112.4	113.7	3900	1563	1576
HB 891529+050	0841481301	2019-08-22	75.3	92.9	93.0	56.3	134.1	134.6	3592	1407	1439
PG1307+085	0841481401	2020-01-22	73.1	86.9	86.8				10547	3971	3787
PG1425+267	0841481501	2020-02-05	73.3	89.9	90.2	63.7	152.2	152.0	4708	2013	2004
PG1352+183	0841481601	2020-01-26	74.4	93.1	93.0	58.3	173.6	171.8	3951	1646	1685
2MASS J105144+3539	0841481701	2020-05-26	80.3	95.3	93.0	41.6	59.1	60.5	2139	811	859
2MASS J0220–0728	0841481901	2020-02-03	77.1	101.9	102.2	57.5	128.1	130.8	3856	1661	1678
LBQS 1338–0038	0841482101	2020-02-01	91.6	114.3	114.4	81.9	202.9	201.3	7775	3085	3139
SUBWAYS targets observed prior AO18 cycle											
PG0804+761	0102040401	2000-11-04	2.33	6.56	6.56		138.9	141.0	1823	845	889
	0605110101	2010-03-10	29.2	27.6	27.6	78.3	270.2	270.1	8426	3070	3316
	0605110201	2010-03-12	25.2	35.1	35.1	67.1	270.2	238.0	5741	3006	2547
PG1416–129	0203770201	2004-07-14	44.3	48.9	49.0	68.9	133.8	134.5	5693	1997	2037
PG1402+261	0400200101	2006-12-21	28.0	16.6	16.6	39.7			1752	674	683
	0830470101	2018-12-17	67.2	75.5	75.5	59.7	201.0	197.8	3894	1347	1531
HB89 1257+286	0204040101	2004-06-06	72.8	85.3	85.4	70.3	185.2	186.6	5374	2125	2011
	0204040201	2004-06-18	79.1	91.9	93.6	57.7	166.2	166.6	3880	1690	1613
	0204040301	2004-07-12	77.4	96.3	96.4	60.5	162.4	163.5	4341	1750	1856
	0304320201	2005-06-27	64.1	76.7	78.6	61.4	152.7	155.8	4211	1605	1551
	0304320301	2005-06-28	46.2	54.1	54.3	45.3	119.5	123.1	2498	953	1001
	0304320801	2006-06-06	47.5	62.3	62.5	54.0	154.1	154.0	3539	1441	1546
PG1114+445	0109080801	2002-05-14	37.0	42.2	42.2	59.2	93.4	92.4	3787	1351	1293
	0651330101	2010-05-19	24.5	29.4	30.0	41.9	54.9	55.4	1922	682	778
	0651330301	2010-05-23	30.3	34.3	34.3	32.2	50.2	51.2	1802	626	627
	0651330401	2010-06-10	29.9	38.0	38.5	36.2	63.7	65.5	1861	853	937
	0651330501	2010-06-14	25.4	29.8	29.6	33.1	55.3	55.1	1843	710	715
	0651330601	2010-11-08	18.5	30.1	30.1	51.6	82.6	83.4	2838	1289	1248
	0651330701	2010-11-16	19.5	26.1	26.1	43.6	68.6	68.6	2137	915	937
	0651330801	2010-11-18	23.6	28.4	29.6	43.9	63.8	63.7	2053	794	857
	0651330901	2010-11-20	22.9	26.9	27.5	45.6	69.3	69.0	2261	906	1000
	0651331001	2010-11-26	21.4	25.1	25.0	41.0	59.9	59.7	1914	658	739
0651331101	2010-12-12	17.1	6.89	6.72	38.7			1672	553	638	

Table D.1: Summary of the phenomenological final best-fitting continuum model parameters of each observation of the SUBWAYS sample, including the iron K emission and absorption lines, with their Gaussians model parameters reported separately in Table 2. The $\mathcal{N}\mathcal{H}\mathcal{M}$ used in Section 4.4 consist of the best-fitting models reported here minus the Gaussian absorption components. Flux in the 4–10 keV band in units of $\text{erg cm}^{-2} \text{s}^{-1}$. Reduced C stat and number of degrees of freedom (ν) for the final best-fit model. All the warm absorber components are required at $P_F > 99\%$. C -stat using the number of bins (ζ) in each EPIC detector and the total C -stat with the degree of freedoms (ν) corresponding to the final best-fit model.

⊠ A narrow (10 eV) Gaussian absorption line of rest-frame energy of $E = 3.51 \pm 0.06$ keV was required at 3σ (99.7%) confidence level.

† Seyfert 2 target with an intrinsic neutral absorber with column density of $\log(N_{\text{H}}/\text{cm}^{-2}) = 23.25^{+0.02}_{-0.02}$ required at P_F VALUE. The soft X-ray band < 2 keV was modelled with two thermal emission components with *apec* yielding $kT_{\text{low}} = 145^{+34}_{-36}$ eV, $\text{norm}_{\text{low}} = 1.7^{+2.3}_{-0.5} \times 10^{-5}$ and $kT_{\text{high}} = 732^{+21}_{-20}$ eV, $\text{norm}_{\text{low}} = 2.3^{+0.9}_{-0.3} \times 10^{-6}$ with normalizations in unit of $\frac{10^{-14}}{4\pi(D_A(1+z))^2} \int n_e n_H dV$ where D_A is the angular diameter distance to the source in cm, n_e and n_H are the electron and H densities (cm^{-3}), respectively. A narrow/strong Gaussian emission line of $E = 2.35 \pm 0.04$ keV was required at 3.6σ ($> 99.9\%$) confidence level.

‡ Intrinsic neutral absorber with $\log(N_{\text{H}}/\text{cm}^{-2}) = 21.83^{+0.01}_{-0.01}$ required at $P_F > 99.99\%$ and two narrow soft X-ray emission at $E_{\text{rest}} = 0.54^{+0.03}_{-0.03}$ keV and $E_{\text{rest}} = 0.75^{+0.02}_{-0.03}$ keV both at $P_F > 99.99\%$

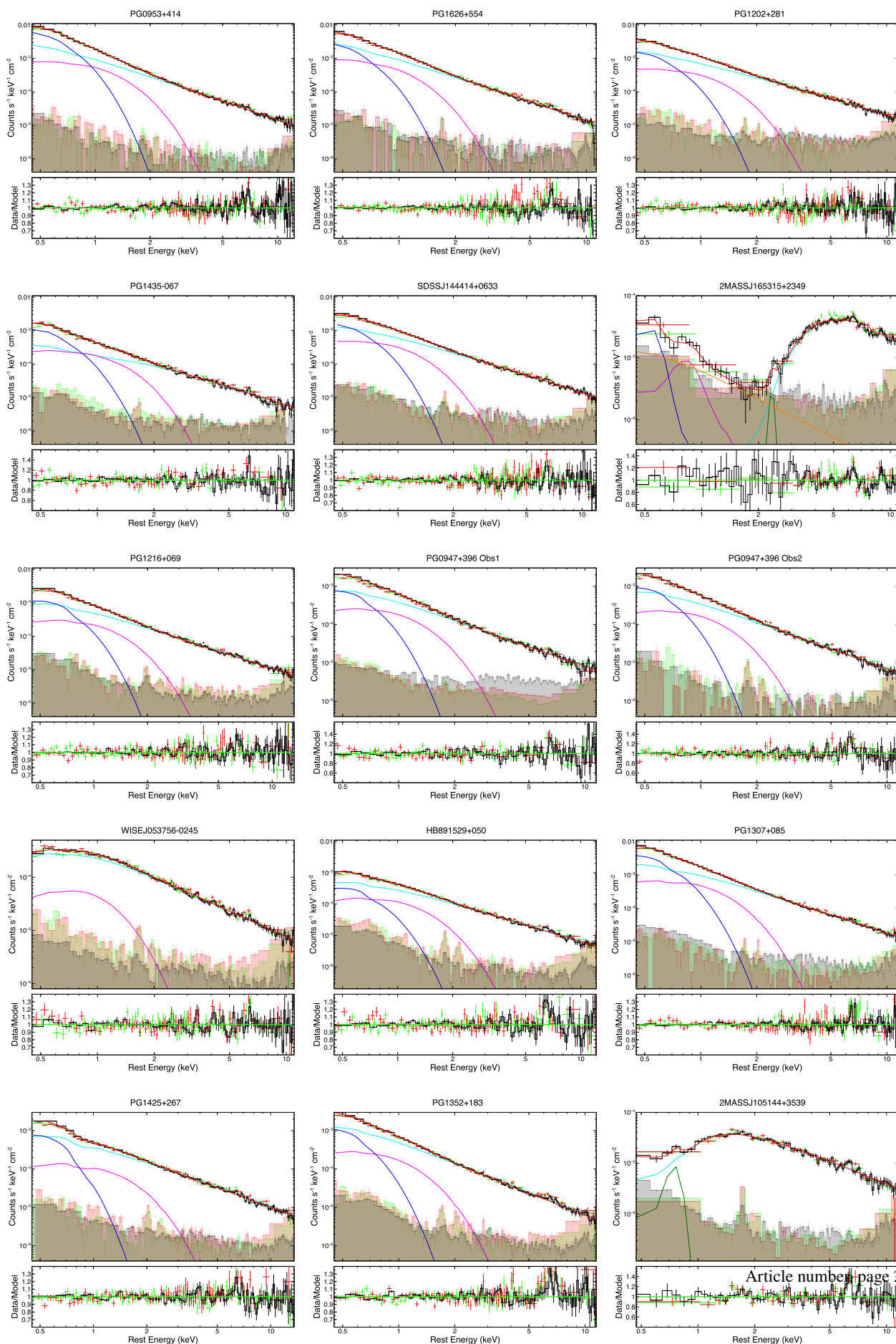
Source	XMM ObsID	Baseline Model: Continuum parameters										Stats				Cross-cal.	
		power-law			bbody _{low}		bbody _{high}		XABS			C_{pn}/ζ	C_{mos1}/ζ	C_{mos2}/ζ	C_{tot}/ν	MOS 1	MOS 2
		Γ	norm 10^{-3}	$F_{4-10\text{keV,obs}}$ 10^{-12}	kT_{low} eV	norm _{low} 10^{-5}	kT_{high} eV	norm _{high} 10^{-5}	N_{H} 10^{21} cm^{-2}	$\log(\xi)$ erg cm s^{-1}	f_{cov} %						
PG0052+251	0841480101	$1.76^{+0.03}_{-0.03}$	$1.71^{+0.48}_{-0.49}$	$4.10^{+0.06}_{-0.06}$	110^{+4}_{-4}	$9.0^{+4.3}_{-2.4}$	248^{+4}_{-4}	$3.2^{+0.8}_{-0.7}$	$6.0^{+1.4}_{-3.4}$	$-1.1^{+0.5}_{-0.4}$	45^{+17}_{-16}	125.7/102	124.4/119	127.0/127	377.1/335	$1.02^{+0.01}_{-0.01}$	$1.04^{+0.01}_{-0.01}$
PG0953+414	0841480201	$1.87^{+0.04}_{-0.04}$	$0.90^{+0.05}_{-0.05}$	$1.81^{+0.04}_{-0.03}$	115^{+3}_{-3}	$8.8^{+0.6}_{+0.5}$	280^{+14}_{-14}	$2.0^{+0.2}_{-0.2}$	$0.88^{+0.20}_{-0.22}$	$1.1^{+0.3}_{-0.2}$	100 ^f	109.7/106	109.7/114	152.5/120	371.8/324	$1.06^{+0.01}_{-0.01}$	$1.08^{+0.01}_{-0.01}$
PG1626+554	0841480401	$1.90^{+0.03}_{-0.03}$	$0.96^{+0.04}_{-0.04}$	$1.80^{+0.03}_{-0.04}$	102^{+5}_{-6}	$4.0^{+0.4}_{-0.4}$	225^{+14}_{-14}	$1.6^{+0.2}_{-0.2}$	$0.86^{+0.23}_{-0.32}$	$0.84^{+0.34}_{-0.23}$	100 ^f	79.0/90	125.2/115	115.1/120	320.1/311	$1.01^{+0.01}_{-0.01}$	$1.05^{+0.01}_{-0.01}$
PG1202+281	0841480501	$1.64^{+0.01}_{-0.01}$	$0.80^{+0.06}_{-0.06}$	$2.43^{+0.04}_{-0.05}$	115^{+7}_{-8}	$2.3^{+0.9}_{-0.4}$	265^{+21}_{-20}	$2.3^{+0.9}_{-0.3}$	$7.4^{+11.1}_{-5.1}$	$0.57^{+0.44}_{-0.53}$	28^{+17}_{-13}	92.1/108	112.6/118	127.0/124	331.8/333	$1.07^{+0.01}_{-0.01}$	$1.08^{+0.01}_{-0.01}$
PG1435–067	0841480601	$1.68^{+0.06}_{-0.07}$	$0.30^{+0.03}_{-0.03}$	$0.80^{+0.03}_{-0.02}$	103^{+4}_{-4}	$1.7^{+0.1}_{-0.1}$	283^{+26}_{-28}	$0.36^{+0.08}_{-0.08}$	–	–	–	86.8/83	124.5/104	159.4/112	370.7/287	$1.02^{+0.02}_{-0.02}$	$1.02^{+0.02}_{-0.02}$
SDSS J144414+0633 [⊠]	0841480701	$1.72^{+0.03}_{-0.03}$	$0.65^{+0.23}_{-0.22}$	$1.64^{+0.03}_{-0.03}$	103^{+5}_{-5}	$2.3^{+0.1}_{-0.1}$	259^{+15}_{-15}	$0.96^{+0.09}_{-0.10}$	–	–	–	117.3/91	117.4/118	124.2/124	358.9/321	$1.02^{+0.01}_{-0.01}$	$1.02^{+0.01}_{-0.01}$
2MASS J165315+2349 [†]	0841480801	$1.65^{+0.09}_{-0.08}$	$1.00^{+0.20}_{-0.20}$	$2.17^{+0.04}_{-0.07}$	–	–	–	–	–	–	–	74.2/82	83.2/100	105.7/107	263.1/273	$1.01^{+0.03}_{-0.03}$	$1.07^{+0.03}_{-0.03}$
PG1216+069	0841480901	$1.74^{+0.01}_{-0.01}$	$0.48^{+0.02}_{-0.02}$	$1.19^{+0.02}_{-0.03}$	117^{+8}_{-7}	$2.6^{+0.3}_{-0.2}$	276^{+21}_{-20}	$0.95^{+0.12}_{-0.12}$	$1.4^{+1.1}_{-0.8}$	$2.0^{+0.3}_{-0.4}$	100 ^f	83.2/89	122.4/114	141.8/121	347.4/311	$1.03^{+0.01}_{-0.01}$	$1.05^{+0.01}_{-0.01}$
PG0947+396 (Obs 1)	0841481001	$1.71^{+0.06}_{-0.07}$	$0.36^{+0.03}_{-0.03}$	$0.93^{+0.03}_{-0.04}$	110^{+9}_{-10}	$1.3^{+0.2}_{-0.2}$	269^{+29}_{-28}	$0.64^{+0.11}_{-0.11}$	–	–	–	96.8/82	102.0/100	108.2/109	307.0/277	$0.99^{+0.02}_{-0.02}$	$1.03^{+0.02}_{-0.02}$
PG0947+396 (Obs 2)	0841482301	$1.73^{+0.05}_{-0.05}$	$0.33^{+0.02}_{-0.02}$	$0.84^{+0.02}_{-0.03}$	108^{+6}_{-6}	$1.5^{+0.1}_{-0.1}$	274^{+22}_{-22}	$0.59^{+0.08}_{-0.08}$	–	–	–	81.1/84	112.5/107	99.7/112	293.2/293	$1.04^{+0.02}_{-0.02}$	$1.04^{+0.02}_{-0.02}$
WISE J053756–0245	0841481101	$1.65^{+0.06}_{-0.06}$	$0.30^{+0.01}_{-0.01}$	$0.91^{+0.02}_{-0.02}$	–	–	228^{+21}_{-20}	$0.17^{+0.04}_{-0.04}$	–	–	–	96.1/86	121.8/109	121.1/114	339.0/301	$1.06^{+0.02}_{-0.02}$	$1.04^{+0.02}_{-0.02}$
HB 891529+050	0841481301	$1.75^{+0.05}_{-0.05}$	$0.31^{+0.02}_{-0.02}$	$0.77^{+0.02}_{-0.03}$	116^{+13}_{-14}	$0.74^{+0.18}_{-0.15}$	275^{+21}_{-20}	$0.42^{+0.07}_{-0.07}$	$0.68^{+0.42}_{-0.45}$	$1.2^{+0.7}_{-0.5}$	100 ^f	84.3/86	112.1/113	129.4/118	325.7/304	$1.04^{+0.01}_{-0.01}$	$1.04^{+0.01}_{-0.01}$
PG1307+085	0841481401	$1.82^{+0.02}_{-0.02}$	$1.10^{+0.04}_{-0.04}$	$2.28^{+0.03}_{-0.03}$	110^{+3}_{-3}	$6.8^{+0.6}_{-0.6}$	260^{+11}_{-11}	$1.8^{+0.1}_{-0.1}$	$0.98^{+0.20}_{-0.19}$	$0.36^{+0.21}_{-0.21}$	100 ^f	114.8/94	116.1/119	186.5/126	399.4/327	$1.05^{+0.01}_{-0.01}$	$1.02^{+0.01}_{-0.01}$
PG1425+267	0841481501	$1.71^{+0.11}_{-0.11}$	$0.42^{+0.05}_{-0.05}$	$1.09^{+0.02}_{-0.02}$	96^{+6}_{-6}	$2.7^{+0.3}_{-0.3}$	321^{+21}_{-20}	$0.60^{+0.9}_{-0.3}$	$7.6^{+2.1}_{-1.8}$	$2.3^{+0.11}_{-0.11}$	100 ^f	97.8/88	102.4/115	107.5/120	307.6/307	$1.03^{+0.01}_{-0.01}$	$1.05^{+0.01}_{-0.01}$
PG1352+183	0841481601	$1.92^{+0.04}_{-0.04}$	$0.45^{+0.03}_{-0.03}$	$0.85^{+0.02}_{-0.03}$	98^{+4}_{-5}	$1.7^{+0.1}_{-0.1}$	244^{+17}_{-17}	$0.55^{+0.08}_{-0.08}$	–	–	–	119.9/88	128.8/115	112.9/119	361.7/311	$1.03^{+0.01}_{-0.01}$	$1.04^{+0.01}_{-0.01}$
2MASS J105144+3539 [‡]	0841481701	$1.56^{+0.02}_{-0.02}$	$0.14^{+0.10}_{-0.05}$	$0.46^{+0.01}_{-0.02}$	–	–	–	–	–	–	–	94.7/80	87.2/94	122.3/102	304.3/263	$1.10^{+0.04}_{-0.04}$	$1.02^{+0.03}_{-0.03}$
2MASS J0220–0728	0841481901	$1.67^{+0.05}_{-0.06}$	$0.29^{+0.07}_{-0.07}$	$0.83^{+0.02}_{-0.01}$	–	–	197^{+11}_{-11}	$0.21^{+0.04}_{-0.04}$	$21.9^{+0.3}_{-0.5}$	$0.58^{+0.44}_{-0.52}$	29^{+14}_{-13}	79.7/78	149.7/114	117.6/119	347.0/311	$1.03^{+0.02}_{-0.02}$	$1.05^{+0.02}_{-0.02}$
LBQS 1338–0038	0841482101	$1.69^{+0.03}_{-0.04}$	$0.26^{+0.02}_{-0.02}$	$1.34^{+0.03}_{-0.03}$	119^{+7}_{-8}	$1.7^{+0.3}_{-0.2}$	282^{+20}_{-20}	$0.71^{+0.09}_{-0.09}$	$0.72^{+0.33}_{-0.32}$	$0.95^{+0.35}_{-0.31}$	100 ^f	101.5/92	128.8/119	100.1/125	330.4/320	$1.02^{+0.01}_{-0.01}$	$1.03^{+0.01}_{-0.01}$

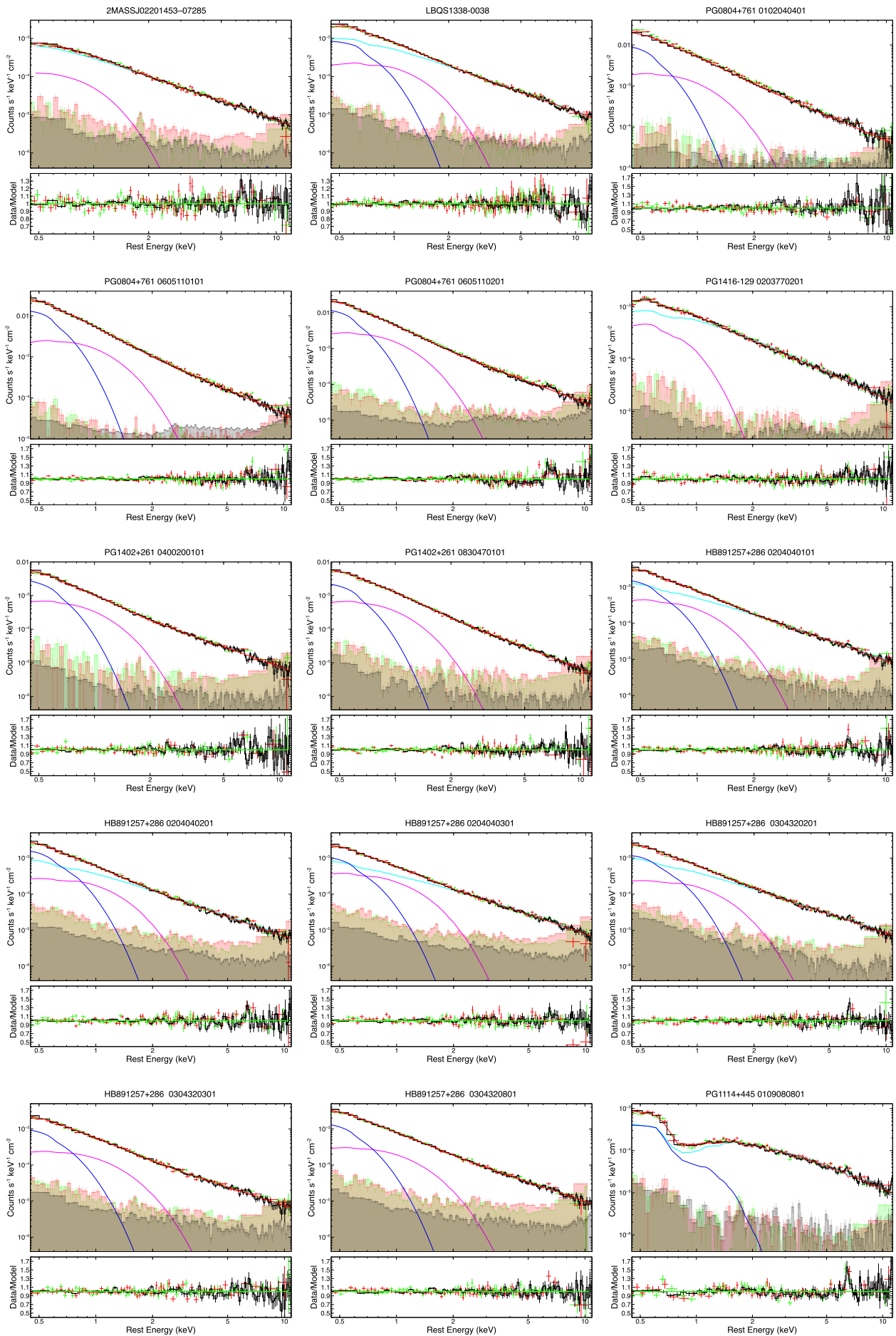
Source	XMM ObsID	Baseline Model: Continuum parameters													Cross-cal.		
		power-law			bbody _{low}		bbody _{high}		XABS			Stats				MOS 1	MOS 2
		Γ	norm 10 ⁻³	$F_{4-10\text{keV,obs}}$ 10 ⁻¹²	kT_{low} eV	norm _{low} 10 ⁻⁵	kT_{high} eV	norm _{high} 10 ⁻⁵	N_{H} 10 ²¹ cm ⁻²	$\log(\xi)$ erg cm s ⁻¹	f_{cov} %	C_{pn}/ζ	C_{mos1}/ζ	C_{mos2}/ζ	C_{tot}/ν		
PG0804+761	0102040401	1.97 ^{+0.05} _{-0.06}	3.93 ^{+0.28} _{-0.29}	6.71 ^{+0.21} _{-0.24}	93 ⁺⁶ ₋₇	3.2 ^{+0.8} _{-0.8}	239 ⁺²⁷ ₋₂₉	0.11 ^{+0.01} _{-0.01}	–	–	–	88.8/92	137.6/112	131.1/112	357.6/302	1.14 ^{+0.02} _{-0.02}	1.16 ^{+0.02} _{-0.02}
	0605110101	1.96 ^{+0.03} _{-0.03}	3.35 ^{+0.15} _{-0.15}	5.67 ^{+0.07} _{-0.06}	92 ⁺² ₋₂	2.1 ^{+0.7} _{-0.8}	252 ⁺¹¹ ₋₁₂	0.48 ^{+0.04} _{-0.04}	–	–	–	116.2/106	153.0/121	131.9/126	401.0/333	1.07 ^{+0.01} _{-0.01}	1.09 ^{+0.01} _{-0.01}
	0605110201	2.08 ^{+0.03} _{-0.03}	3.03 ^{+0.11} _{-0.11}	4.23 ^{+0.08} _{-0.07}	85 ⁺³ ₋₃	1.7 ^{+0.7} _{-0.8}	200 ⁺¹² ₋₁₂	0.41 ^{+0.04} _{-0.04}	–	–	–	129.9/103	133.6/124	139.6/120	403.0/30	1.04 ^{+0.01} _{-0.01}	1.09 ^{+0.01} _{-0.01}
PG1416–129*	0203770201	1.74 ^{+0.02} _{-0.02}	0.69 ^{+0.17} _{-0.18}	2.28 ^{+0.02} _{-0.04}	153 ⁺⁷ ₋₈	1.0 ^{+0.2} _{-0.3}	–	–	1.20 ^{+0.05} _{-0.05}	0.80 ^{+0.51} _{-0.27}	100 ^f	132.5/109	120.5/118	136.5/118	389.6/335	1.53 ^{+0.02} _{-0.01}	1.06 ^{+0.02} _{-0.01}
PG1402+261	0400200101	2.00 ^{+0.05} _{-0.05}	0.63 ^{+0.04} _{-0.04}	1.00 ^{+0.03} _{-0.02}	90 ⁺⁵ ₋₅	4.2 ^{+0.3} _{-0.3}	213 ⁺¹⁸ ₋₁₈	1.0 ^{+0.1} _{-0.1}	–	–	–	94.7/99	90.0/106	117.2/108	301.9/301	1.04 ^{+0.02} _{-0.01}	1.09 ^{+0.02} _{-0.01}
	0830470101	2.16 ^{+0.05} _{-0.05}	0.79 ^{+0.04} _{-0.04}	0.90 ^{+0.02} _{-0.02}	88 ⁺³ ₋₅	3.9 ^{+0.3} _{-0.3}	217 ⁺¹³ ₋₁₃	1.1 ^{+0.1} _{-0.1}	–	–	–	122/104	136.4/116	107.0/121	365.3/329	1.03 ^{+0.01} _{-0.01}	1.05 ^{+0.01} _{-0.01}
HB89 1257+286	0204040101	1.83 ^{+0.02} _{-0.02}	0.59 ^{+0.47} _{-0.17}	1.20 ^{+0.02} _{-0.03}	102 ⁺⁵ ₋₄	2.1 ^{+0.5} _{-0.3}	229 ⁺¹⁸ ₋₁₅	0.89 ^{+0.39} _{-0.28}	6.00 ^{+4.33} _{-3.71}	-0.14 ^{+0.40} _{-0.63}	35 ⁺¹⁵ ₋₆	117.2/98	121.7/119	137.5/120	376.4/322	1.03 ^{+0.01} _{-0.01}	1.05 ^{+0.01} _{-0.01}
	0204040201	1.83 ^{+0.04} _{-0.04}	0.41 ^{+0.03} _{-0.03}	0.87 ^{+0.03} _{-0.03}	105 ⁺⁵ ₋₅	2.0 ^{+0.3} _{-0.3}	243 ⁺²⁰ ₋₂₀	0.56 ^{+0.08} _{-0.09}	1.00 ^{+0.35} _{-0.35}	-0.27 ^{+0.45} _{-0.45}	100 ^f	111.0/96	151.3/117	157.8/117	420.1/318	1.03 ^{+0.01} _{-0.01}	1.06 ^{+0.01} _{-0.01}
	0204040301	1.87 ^{+0.08} _{-0.09}	0.52 ^{+0.08} _{-0.08}	1.00 ^{+0.02} _{-0.04}	100 ⁺⁷ ₋₇	2.0 ^{+0.9} _{-0.9}	222 ⁺²⁴ ₋₁₉	1.2 ^{+1.1} _{-0.7}	13.35 ^{+0.70} _{-0.83}	-0.52 ^{+0.67} _{-0.83}	52 ⁺¹⁵ ₋₂₇	85.4/96	165.7/119	130.7/119	381.8/319	1.05 ^{+0.01} _{-0.01}	1.05 ^{+0.01} _{-0.01}
	0304320201	1.78 ^{+0.05} _{-0.05}	0.45 ^{+0.03} _{-0.03}	1.05 ^{+0.02} _{-0.03}	113 ⁺⁶ ₋₇	1.3 ^{+0.3} _{-0.2}	256 ⁺²⁷ ₋₂₉	0.47 ^{+0.09} _{-0.09}	0.88 ^{+0.29} _{-0.35}	0.60 ^{+0.31} _{-0.45}	100 ^f	93.9/94	104.5/115	91.4/116	289.9/312	1.03 ^{+0.01} _{-0.01}	1.05 ^{+0.01} _{-0.01}
	0304320301	1.75 ^{+0.06} _{-0.06}	0.39 ^{+0.07} _{-0.07}	0.93 ^{+0.02} _{-0.03}	105 ⁺⁶ ₋₇	0.96 ^{+0.11} _{-0.11}	266 ⁺²⁴ ₋₂₅	0.43 ^{+0.08} _{-0.08}	–	–	–	78.7/91	107.4/112	119.9/113	305.1/306	1.02 ^{+0.02} _{-0.01}	1.05 ^{+0.02} _{-0.01}
	0304320801	1.82 ^{+0.06} _{-0.05}	0.58 ^{+0.03} _{-0.04}	1.25 ^{+0.03} _{-0.03}	100 ⁺⁷ ₋₆	0.51 ^{+0.19} _{-0.3}	262 ⁺²² ₋₂₃	0.34 ^{+0.18} _{-0.18}	–	–	–	101.2/93	100.0/112	110.7/112	311.9/307	1.03 ^{+0.01} _{-0.01}	1.03 ^{+0.01} _{-0.01}
PG1114+445	0109080801	1.98 ^{+0.03} _{-0.03}	1.09 ^{+0.02} _{-0.02}	1.54 ^{+0.04} _{-0.03}	153 ⁺¹² ₋₁₇	1.8 ^{+0.5} _{-0.8}	–	–	73.01 ^{+0.20} _{-0.27}	3.00 ^{+0.03} _{-0.07}	100 ^f	118.7/104	110.5/108	122.0/99	351.1/297	1.09 ^{+0.02} _{-0.02}	1.04 ^{+0.02} _{-0.02}
	0651330101	1.71 ^{+0.15} _{-0.12}	0.58 ^{+0.20} _{-0.12}	1.30 ^{+0.04} _{-0.03}	110 ⁺¹¹ ₋₁₀	2.1 ^{+1.5} _{-1.1}	–	–	16.69 ^{+0.04} _{-0.04}	1.03 ^{+0.04} _{-0.08}	100 ^f	88.0/95	92.8/97	107.5/101	288.3/278	1.11 ^{+0.04} _{-0.04}	1.11 ^{+0.04} _{-0.04}
									91.65 ^{+30.22} _{-31.72}	2.78 ^{+0.99} _{-0.13}							
	0651330301	1.84 ^{+0.39} _{-0.11}	0.76 ^{+0.31} _{-0.15}	1.23 ^{+0.06} _{-0.11}	122 ⁺¹³ ₋₁₀	3.2 ^{+1.3} _{-0.1}	–	–	16.85 ^{+0.86} _{-0.66}	0.70 ^{+0.18} _{-0.11}	100 ^f	86.0/96	92.2/91	112.2/95	290.3/268	1.12 ^{+0.04} _{-0.04}	1.07 ^{+0.04} _{-0.04}
									124.97 ^{+6.41} _{-3.73}	3.00 ^{+0.03} _{-0.09}							
	0651330401	1.91 ^{+0.12} _{-0.14}	0.90 ^{+0.23} _{-0.21}	1.42 ^{+0.07} _{-0.06}	119 ⁺¹⁴ ₋₁₂	2.3 ^{+1.0} _{-0.1}	–	–	27.96 ^{+5.34} _{-3.4}	0.85 ^{+0.16} _{-0.14}	100 ^f	113.1/96	103.1/96	106.4/106	323.1/288	1.09 ^{+0.03} _{-0.03}	1.07 ^{+0.03} _{-0.03}
									79.90 ^{+5.02} _{-3.08}	3.01 ^{+0.08} _{-0.10}							
	0651330501	1.90 ^{+0.12} _{-0.09}	0.97 ^{+0.25} _{-0.17}	1.48 ^{+0.06} _{-0.11}	89 ⁺⁵ ₋₅	1.9 ^{+1.4} _{-0.6}	–	–	19.07 ^{+3.32} _{-3.2}	0.87 ^{+0.15} _{-0.13}	100 ^f	95.0/96	115.8/97	127.4/101	338.2/286	1.07 ^{+0.04} _{-0.04}	1.04 ^{+0.04} _{-0.04}
									98.80 ^{+197.53} _{-33.58}	3.00 ^{+0.22} _{-0.15}							
	0651330601	1.88 ^{+0.07} _{-0.07}	1.38 ^{+0.45} _{-0.43}	2.31 ^{+0.05} _{-0.09}	139 ⁺¹⁵ ₋₁₄	3.29 ^{+1.1} _{-1.1}	–	–	15.81 ^{+0.70} _{-0.70}	-0.17 ^{+0.20} _{-0.20}	100 ^f	112.0/98	135.3/106	122.3/109	369.7/300	1.07 ^{+0.03} _{-0.03}	1.05 ^{+0.03} _{-0.02}
66.08 ^{+33.18} _{-28.45}									2.95 ^{+0.08} _{-0.09}								
0651330701	1.90 ^{+0.10} _{-0.10}	1.12 ^{+0.23} _{-0.20}	1.75 ^{+0.05} _{-0.07}	112 ⁺¹⁴ ₋₁₃	2.6 ^{+1.1} _{-1.0}	–	–	16.70 ^{+0.21} _{-0.08}	0.92 ^{+0.12} _{-0.11}	100 ^f	113.0/97	102.9/101	123.3/105	339.4/291	1.06 ^{+0.03} _{-0.03}	1.06 ^{+0.03} _{-0.03}	
								91.24 ^{+28.70} _{-25.79}	2.86 ^{+0.15} _{-0.11}								
0651330801	1.95 ^{+0.11} _{-0.11}	1.03 ^{+0.26} _{-0.20}	1.47 ^{+0.04} _{-0.09}	102 ⁺¹⁴ ₋₁₃	1.5 ^{+1.1} _{-1.0}	–	–	16.69 ^{+0.41} _{-0.08}	0.81 ^{+0.12} _{-0.10}	100 ^f	85.6/96	83.8/100	134.6/104	304.0/288	1.04 ^{+0.03} _{-0.03}	1.03 ^{+0.03} _{-0.03}	
								119.34 ^{+31.03} _{-32.14}	2.89 ^{+0.14} _{-0.13}								
0651330901	1.80 ^{+0.10} _{-0.09}	0.88 ^{+0.19} _{-0.14}	1.72 ^{+0.04} _{-0.08}	108 ⁺¹⁴ ₋₁₃	3.3 ^{+1.1} _{-1.0}	–	–	18.16 ^{+0.53} _{-0.21}	0.89 ^{+0.17} _{-0.13}	100 ^f	96.0/96	65.3/101	113.2/105	274.2/290	1.12 ^{+0.03} _{-0.03}	1.11 ^{+0.03} _{-0.03}	
								85.35 ^{+27.47} _{-27.47}	2.93 ^{+0.13} _{-0.13}								
0651331001	1.75 ^{+0.10} _{-0.09}	0.69 ^{+0.19} _{-0.14}	1.49 ^{+0.05} _{-0.06}	106 ⁺¹⁴ ₋₁₃	3.3 ^{+1.1} _{-1.0}	–	–	16.77 ^{+0.38} _{-0.06}	0.93 ^{+0.10} _{-0.13}	100 ^f	92.4/95	91.1/98	78.7/103	262.2/284	1.08 ^{+0.04} _{-0.04}	1.07 ^{+0.04} _{-0.03}	
								71.07 ^{+34.65} _{-21.34}	2.99 ^{+0.07} _{-0.12}								
0651331101	1.84 ^{+0.12} _{-0.10}	0.94 ^{+0.24} _{-0.19}	1.60 ^{+0.05} _{-0.08}	109 ⁺¹³ ₋₁₃	2.1 ^{+1.0} _{-1.0}	–	–	16.78 ^{+0.38} _{-0.06}	1.00 ^{+0.10} _{-0.13}	100 ^f	112.2/94	72.7/98	122.0/102	306.9/282	0.99 ^{+0.04} _{-0.03}	1.05 ^{+0.04} _{-0.04}	
								92.09 ^{+36.90} _{-31.35}	2.90 ^{+0.15} _{-0.17}								
									16.57 ^{+0.31} _{-0.11}	0.85 ^{+0.17} _{-0.13}							

Appendix E: Blind-line search results

As in [Figure 4](#), we shown the residual (top) and blind-scan search contours (bottom) for the remaining 39 in [Appendix E.1](#).

Fig. D.1: Broadband fitting and Fe K residuals of the *XMM-Newton* observations in the SUBWAYS sample. The EPIC-pn (black), MOS 1 (red) and MOS 2 (green) spectra the corresponding background spectra (shaded area) and the best-fit model (solid red) are plotted. The individual model components are: absorbed power-law (cyan), black-body low (blue) and high (magenta) kT , soft X-ray Gaussian lines (dark green) and scattered power-law (orange). EPIC-MOS are visually binned to 10σ for clarity.





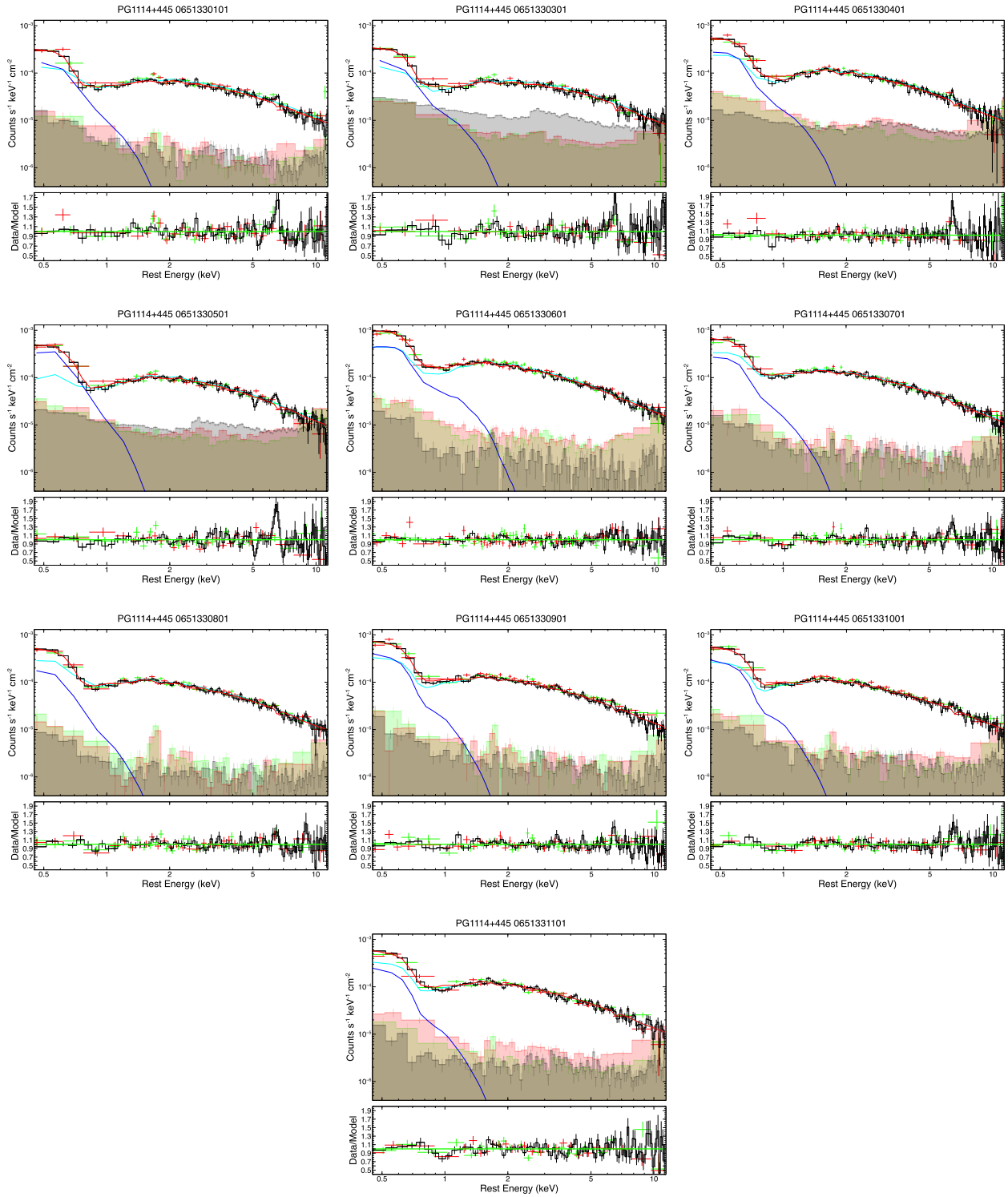


Fig. E.1: Blind line search results, as in Figure 4, for the SUBWAYS sample with the corresponding residuals of the EPIC-pn spectrum in the rest-frame energy between 5–10 keV.

